UNIVERSITY OF STUTTGART

MASTER THESIS

Dual-Species Atomic Beam Source for Lithium and Rubidium

Author:
Raphael BENZ

Supervisor:
Viraatt ANASURI

1st Examiner:
Prof. Dr. Tilman PFAU

2nd Examiner:
Prof. Dr. Martin DRESSEL

A thesis submitted in fulfillment of the requirements for the degree of Master of Science in Physics

in the

Faculty 8 · Mathematics and Physics
5th Institute of Physics

October 4, 2024

Declaration of Authorship

I, Raphael BENZ, declare that this thesis titled, "Dual-Species Atomic Beam Source for Lithium and Rubidium" and the work presented in it are my own. I confirm that:

- I have written this work independently.
- I did not used any sources other than those indicated and that all statements taken verbatim or in spirit from other works, it is marked as such.
- The submitted work has not been the subject of any other examination procedure, neither in its entirety nor in essential parts.
- This work has not already been published either in full or in part. unless the board of examiners has previously approved the publication,
- The content of the electronic copy is the same as that of the printed copy.
- When using IT/AI-supported writing tools, these tools were listed fully with their product name, my source of supply and an overview of the range of functions used in the context of this work. In the creation of this thesis, I worked independently and controlled the use of IT/AI-supported writing tools.
  - A grammar check of the entire work was done using the GPT-4o model ChatGPT, operated by OpenAI Inc.. In a few cases, the tool has slightly rewritten some sentences to improve clarity, without changing its content. *I confirm, that this tool was only used to correct language, and never to generate content. The output was always used as a mere recommendation*. The following (german) command was used: "Ich sende dir Stück für Stück einen selbstgeschrieben englischen Text in latex format. Ich möchte dass du die Struktur, den Stil und den Inhalt gleich lässt. Du sollst mir bitte lediglich grammatikalische Fehler korrigieren und, falls ein Satz sehr schlecht geschrieben ist, ihn leicht umschreiben. Alle anderen Sätze sollen bleiben wie sie sind."

Signed: _____

Date: _____

UNIVERSITY OF STUTTGART

Zusammenfassung

Faculty 8 · Mathematics and Physics
5th Institute of Physics

Master of Science in Physics

Dual-Species Atomic Beam Source for Lithium and Rubidium

by Raphael BENZ

In dieser Arbeit wird eine effusive Atomstrahlquelle für die Erzeugung eines überlagerten Atomstrahls aus Lithium und Rubidium vorgestellt. Mit Hilfe der linearen Absorptionsspektroskopie der D_2-Linie werden der Gesamtfluss der Atome und die Strahldivergenz beider Elemente untersucht. Die Quelle besteht aus zwei getrennten Reservoirs und ist so konzipiert, dass sie entweder im unabhängigen Einzelspeziesbetrieb für jedes Element oder im kombinierten Doppelspeziesbetrieb arbeitet. Im Einzelspeziesbetrieb beträgt der Gesamtfluss des fermionischen Lithiumisotops ^{6}Li $1{,}3 \cdot 10^{16}\,\mathrm{s}^{-1}$ bei einer Reservoirtemperatur von 450 °C, mit einem $1/e^2$ Divergenzwinkel von $2 \cdot 574$ mrad. Dies würde zu einer geschätzten MOT-Laderate von $1{,}7 \cdot 10^{10}\,\mathrm{s}^{-1}$ und einer Lebensdauer der Quelle von etwa 15 000 Stunden führen. Der Gesamtfluss des bosonischen Rubidium-Isotops ^{87}Rb beträgt $3{,}3 \cdot 10^{10}\,\mathrm{s}^{-1}$ bei einer Reservoirtemperatur von 120 °C, mit einem Divergenzwinkel von $2 \cdot 10$ mrad. Dies würde zu einer geschätzten MOT-Laderate von $9{,}6 \cdot 10^{8}\,\mathrm{s}^{-1}$ und einer Lebensdauer der Quelle von etwa 3900 Stunden führen. Beim Betrieb mit zwei Spezies muss ein Kompromiss zwischen einem höheren Rubidiumfluss und einem höheren Lithiumfluss gefunden werden. Eine geschätzte MOT-Laderate von mindestens $4{,}8 \cdot 10^{8}\,\mathrm{s}^{-1}$ für ^{87}Rb und mindestens $2{,}7 \cdot 10^{9}\,\mathrm{s}^{-1}$ für ^{6}Li ist gleichzeitig möglich.

UNIVERSITY OF STUTTGART

Abstract

Faculty 8 · Mathematics and Physics
5th Institute of Physics

Master of Science in Physics

Dual-Species Atomic Beam Source for Lithium and Rubidium

by Raphael BENZ

In this thesis, an effusive atomic beam source for the generation of an overlapping beam of lithium and rubidium is presented. Linear absorption spectroscopy on the D_2 line is performed to probe the total flux of atoms and the beam divergence of both species. The source consist of two separate reservoirs and is designed to operate either in an independent single-species operation for each element or in combined dual-species operation. In single-species operation, the total flux of the fermionic lithium isotope ^{6}Li is determined to be $1.3 \cdot 10^{16}\,\mathrm{s}^{-1}$ at a reservoir temperature of 450 °C, with a $1/e^2$ divergence angle of $2 \cdot 574$ mrad. This would result in an estimated MOT loading rate of $1.7 \cdot 10^{10}\,\mathrm{s}^{-1}$ and a source lifetime of 15 000 hours. The total flux of the bosonic rubidium isotope ^{87}Rb is determined to be $3.3 \cdot 10^{10}\,\mathrm{s}^{-1}$ at a reservoir temperature of 120 °C, with a total divergence angle of $2 \cdot 10$ mrad. This would result in an estimated MOT loading rate of $9.6 \cdot 10^{8}\,\mathrm{s}^{-1}$ and a source lifetime of 3900 hours. In dual-species operation, a trade-off must be made between achieving a higher rubidium flux or a higher lithium flux. An estimated MOT loading rate of at least $4{,}8 \cdot 10^{8}\,\mathrm{s}^{-1}$ for ^{87}Rb and at least $2.7 \cdot 10^{9}\,\mathrm{s}^{-1}$ for ^{6}Li is possible simultaneously.

Contents

Chapter 1

Introduction

Strongly Interacting Fermi Gases appear in nature from the smallest to the largest scales. Even in the absence of interactions, the Pauli exclusion principle induces strong quantum correlations in these systems [1]. A key role in such systems is played by *Polarons*, which are quasi-particle excitations around an impurity that strongly interacts with the surrounding bath, significantly altering the overall properties of the system [2]. Such phenomena are of central importance in modern research, as polaron-polaron interactions are believed to lead to the macroscopic quantum behavior in exotic materials, such as high temperature superconductors and strange metals [3]. These systems however are extremely difficult to model theoretically [4]. In 1982, Richard Feynman first proposed the idea of using a well-controlled quantum system to simulate the dynamics of another, intractable system, a concept now known as *Quantum Simulation* [5]. In recent years, quantum simulations of such systems using ultra-cold atoms and quantum gas microscopy have gained increasing importance in this field. Major advances have been made in the field of strongly interacting Fermi gases, including the observation of anti-ferromagnetic correlations [6] and transport phenomena in a bad metal [7]. However, the interactions in these systems have so far been limited to short-ranged, Van-der-Waals type interactions. Since Bose gases with long-range dipolar interactions have shown many intriguing properties, such as quantum droplets and supersolidity [8], developing novel experimental tools to study Fermi gases with long-range interactions, such as atom-charge interactions, would greatly expand the range of accessible physics.

One such experimental tool to study these phenomena is the *Pulsed Ion Microscope* in Stuttgart [9], which enables the detection of charged particles beyond the optical diffraction limit with high resolution in an environment with excellent electric field control. In recent years, this apparatus was operated with rubidium to investigate the physics of Rydberg atom - ion systems. In 2022, a novel molecular bond between an ion and a Rydberg atom was discovered [10], and the high spatial ($< 200\,\mathrm{nm}$) and temporal ($< 10\,\mathrm{ns}$) resolution of the ion microscope, with its $100\,\mu\mathrm{m}$ depth of field, allowed for the direct observation of the vibrational dynamics of these molecules [11]. Recent studies have also explored the dynamics of strongly polar atom-ion scattering [12].

The high spatial and temporal resolution of the ion microscope, combined with its capability for three-dimensional imaging, makes it an ideal tool for studying strongly interacting Fermi gases. Of particular interest will be the dynamics of a *Charged Polaron* in a Fermi gas, which serves as a versatile tool for investigating strongly-coupled open quantum systems. The excellent electric field control allows the creation of a single ion immersed in a Fermi gas, which enables the study of these polarons.

Since all accessible stable rubidium isotopes are bosons, the ion microscope setup must be extended to the usage of a fermionic atom. The lithium isotope ^{6}Li is used,

because it's proposed that due to its low mass the yet untested s-wave scattering regime in ion-atom interactions can be reached [13, 14]. However, due to the significant successes achieved with rubidium in recent years, and the prospects of other intriguing projects such as heteronuclear Rydberg atom - ion molecules, the setup should retain its capability to operate with rubidium. Therefore, a dual-species ultra-cold atom experiment is required. A design based on the work of Stamper-Kurn and Madison [15, 16] has been adopted, where a single atomic beam source containing both species produces an overlapping atomic beam, which is slowed by a common Zeeman slower and captured in a magneto-optical trap. The common Zeeman slower and MOT chamber design have been already implemented in the current ion microscope setup [17]. The next step is to build a *Dual-Species Atomic Beam Source*, which will be the focus of this work.

During this thesis, a dual-species atomic beam source for lithium and rubidium was constructed and characterized by using linear absorption spectroscopy. The two key quantities extracted from the measurements are the *Beam Divergence* and the *Total Flux*, since these quantities determine the loading rate of atoms into the magneto-optical trap.

This thesis is structured as follows: In chapter 2, the theoretical basics necessary to understand this work are explained. This includes a description of the working principle of a single-species atomic beam source and a brief overview of the basics of atom-light interaction required for the spectroscopic characterization of the atomic beam. Building on this, the general design concept of the dual-species source is presented in chapter 3, along with its experimental realization. Then, in Chapter 4, the results of the spectroscopic characterization of an atomic beam are discussed. First, each beam is characterized in single-species operation to confirm that they are functioning as expected. Finally, the overlapping beam of both elements is investigated. Chapter 5 concludes the thesis with a brief summary and outlook on future improvements of the source.

Chapter 2

Theoretical Basics

In this chapter, the theoretical basics which are necessary for the understanding and characterization of an effusive atomic beam source are introduced. First, in section 2.1, the working principle of a single-species atomic beam source is explained. Then, a brief overview of the basics of atom-light interaction necessary for the characterization of the atomic beam via linear absorption spectroscopy is provided. Finally, in section 2.3, the most important properties and numerical values for lithium and rubidium are summarized.

2.1 Effusive atomic beam source

An *atomic beam* is a spatially well-defined and directed flow of atoms [18]. The starting point of a single-species atomic beam source is an evacuated reservoir containing the solid or liquid source material with atomic mass m at temperature T, where it is in equilibrium with its vapor with temperature dependent vapor pressure p. The reservoir has a small[1] cylindrical orifice with diameter $d = 2r$ and length L, through which a small fraction of atoms effuse, forming a directed beam of atoms. The properties of this atomic beam are discussed in the following.

Basic properties of the vapor The atomic density of the vapor can be approximated by the classical ideal gas law [19]

$$n = \frac{p}{k_\mathrm{B} T}, \tag{2.1}$$

where k_B is the Boltzmann constant. The velocities v of the atoms in the reservoir follow the Maxwell-Boltzmann distribution [19]

$$f(v) = \frac{4}{\sqrt{\pi}} \frac{v^2}{\hat{v}^3} \exp\left(-\frac{v^2}{\hat{v}^2}\right), \tag{2.2}$$

with the most-probable velocity [19]

$$\hat{v} = \sqrt{\frac{2k_\mathrm{B}T}{m}}. \tag{2.3}$$

The average velocity is given by [19]

$$\bar{v} = \sqrt{\frac{8k_\mathrm{B}T}{\pi m}}. \tag{2.4}$$

[1] Small means that the area of the opening is small compared to the surface area of the reservoir

Collisions between atoms can be modeled by two-body van der Waals interactions with the interaction potential $V(r) = C_6/r^6$, where C_6 is a species-dependent coefficient and r is the relative distance between the atoms. The total *collisional cross section* can be calculated using [20]

$$\sigma = \frac{9\pi}{4}\left(\frac{3\pi}{16}\right)^{2/5}\left(\frac{2C_6}{v_{\mathrm{rel}}}\right)^{2/5}, \tag{2.5}$$

where σ, C_6 and v_{rel} are each given in atomic units. v_{rel} is the average relative velocity, which is $\sqrt{2}\bar{v}$ for a Maxwell-Boltzmann distributed vapor. The *mean collision-free path* is given by [19]

$$\bar{l} = \frac{1}{\sqrt{2}n\sigma}. \tag{2.6}$$

Flow regimes The properties of the atomic beam strongly depend on the flow regime in the orifice. Two distinct regimes are distinguished [18]: *Molecular flow* and *continuum flow*. Molecular flow occurs when the mean free path of the atoms is larger than the spatial dimensions of the orifice. In this regime, collisions between atoms are rare compared to collisions between a single atom and the orifice wall, meaning the atoms move independent of each other. In contrast, in the continuum flow regime, the mean free path is smaller than the orifice dimensions, leading to frequent collisions between atoms. The flow has a hydrodynamic character, which can be either turbulent or laminar. The transition between these two flow regimes, where the mean free path is on the order of the orifice dimension, is continuous and is called the transition flow regime [18].

An atomic beam source that operates in the molecular flow regime is called an *effusive atomic beam source* [18]. The characteristics of such a beam can be analytically calculated using gas kinetics. In the following, molecular flow is assumed.

Effusion from thin-walled orifice We first consider the case where the orifice length is small compared to its diameter. In this case, most atoms are effused directly from the reservoir without hitting the orifice walls and the calculations are simplified using the approximation $L = 0$.

The number of atoms per unit time (called *flux*), $d\phi$, with a velocity in the range $[v, v + dv]$, effused from a surface element dA of the orifice into the unit angle $d\Omega$, can be calculated by simple gas kinetics as [19, 21]

$$d\phi = nv\cos(\theta)\, dA \cdot f(v)dv \cdot \frac{d\Omega}{4\pi}, \tag{2.7}$$

where $\theta \in [0, \pi/2]$ is the angle between $d\Omega$ and the normal of dA. A sketch of the geometry is shown in Fig. 2.1a. Integration over all velocities in the beam simplifies Eq. 2.7 to

$$d\phi = n\bar{v}\cos(\theta)\, dA \cdot \frac{d\Omega}{4\pi}. \tag{2.8}$$

The flux at an arbitrary point downstream of the orifice follows from integrating Eq. 2.8 over the total area of the orifice [18]. A general analytical integration is only possible in a few symmetrical special cases [22]. Since we are interested in the

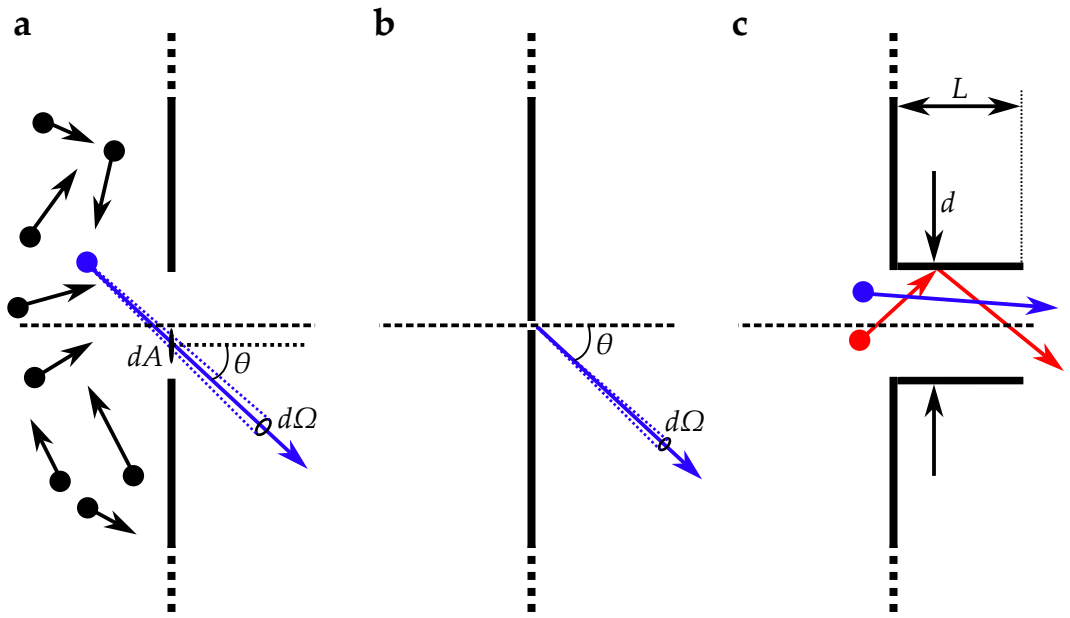

FIGURE 2.1: **a** An atom (blue) effuses out of a thermal reservoir of atoms (black) through a surface element dA of an infinitely thin orifice into a solid angle $d\Omega$ at an angle θ relative to the normal of dA. **b** At large distances from the orifice, it can be approximated as effectively point-like, reducing θ to the angle between $d\Omega$ and the axis of the orifice. **c** Effusion through a cylindrical tube with length L and diameter d. Atoms can effuse directly from the reservoir (blue) or via diffuse scattering from the orifice wall (red).

far-field of the beam[2], we can approximate the source as effectively point-like by replacing dA in Eq. 2.8 with the orifice area $A = \pi r^2$ [18]:

$$d\phi = n\bar{v}A\cos(\theta)\cdot\frac{d\Omega}{4\pi}. \tag{2.9}$$

Here, θ reduces to the angle between $d\Omega$ and the symmetry axis of the orifice (see Fig. 2.1b). The flux has a $\cos(\theta)$ *angular distribution* and is rotationally symmetric around the axis of the orifice. The *total flux* of atoms effused from the source follows from the integration of Eq. 2.9 over the entire solid angle, using the unit angle in spherical coordinates, $d\Omega = 2\pi\sin(\theta)\,d\theta$:

$$\phi = \frac{1}{4}n\bar{v}A. \tag{2.10}$$

Effusion from cylindrical tube Now, consider the case of a cylindrical tube with non-negligible length. The atomic beam now consists of two contributions: first, atoms that are directly effused from the reservoir without hitting the orifice wall, and second, atoms that have collided with the wall [18], as shown in Fig. 2.1c. For the latter, a diffuse scattering from the wall is assumed. The $\cos(\theta)$ angular distribution of atoms from the thin-walled orifice is modified by an additional correction

[2]Distance from orifice large compared to its dimensions

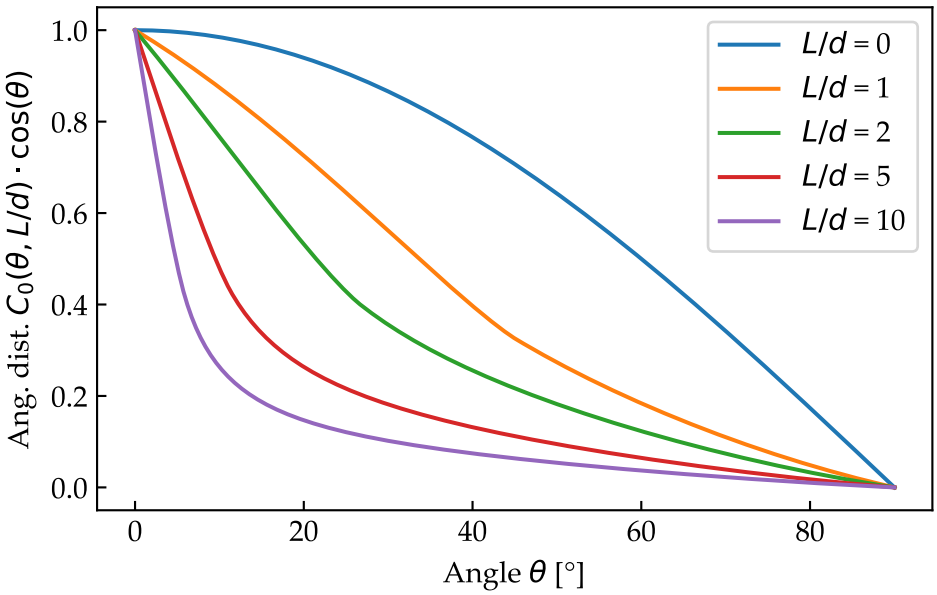

FIGURE 2.2: Angular distribution $C_0(\theta, L/d) \cdot \cos(\theta)$ for a cylindrical orifice with length L and diameter d.

factor $C_0(\theta,L/d)$ which depends explicitly on the aspect ratio of the tube [18]. The exact analytical expression is given in Appendix A. An example of the angular distribution for orifices with different aspect ratios is shown in Fig. 2.2. Tubes with larger aspect ratios have a smaller beam divergence, thus they act as a collimator. To quantify the divergence of the beam, one can define a *divergence angle* as twice the angle at which the angular distribution drops to $1/e^2$, in analogy to the divergence defined for a Gaussian light beam.

The total flux is also modified due to random diffusion of atoms from the orifice wall back into the reservoir [19]. The total flux in Eq. 2.10 is modified by the so-called Clausing factor $1/\kappa$:

$$\phi = \frac{1}{\kappa}\frac{1}{4} n A \bar{v}. \tag{2.11}$$

The Clausing factor depends on the geometry of the orifice and is given by

$$\frac{1}{\kappa} = \frac{8r}{3l} \tag{2.12}$$

for a long cylindrical tube with $L \gg r$. The Clausing factor represents the probability of an atom to directly exit the orifice without returning to the reservoir [23].

2.2 Atom-light interaction

In this section, a brief introduction into atom-light interaction is provided. A semi-classical approach is presented [24], where a quantum-mechanically described atom with discrete eigenstates interacts with a classical monochromatic plane wave, characterized by electric field amplitude E_0, frequency ω and unit polarization vector $\vec{\epsilon}$. The wavelength $\lambda = 2\pi c/\omega$ is given by the usual dispersion of light, where c is the

speed of light. The dominant interaction is the electric dipole interaction with interaction Hamiltonian given by $H_{\text{int}} = -\vec{d} \cdot \vec{E}$. Here, $\vec{E}$ is the electric field vector and $\vec{d} = -e\vec{r}$ is the dipole operator, where e is the electric charge and $\vec{r}$ the position operator. This interaction can be understood as the absorption and emission of individual photons by the atom, thereby changing its state, while neglecting the backreaction on the light field in the semi-classical approach.

Two-level atom For simplicity, consider first a non-moving two-level atom with ground state $|g\rangle$ and excited state $|e\rangle$ separated by an energy difference $\hbar\omega_0$, where $\hbar$ is the reduced Planck's constant and ω_0 is the atomic resonance frequency. An atom in the excited state can spontaneously decay into the ground state by emitting a photon, with the *natural decay rate* [24]

$$\Gamma = \frac{\omega_0^3}{3\pi\epsilon_0\hbar c^3}|\vec{d}_{\text{eg}}|^2. \tag{2.13}$$

Here, ϵ_0 is the vacuum permittivity and

$$\vec{d}_{\text{eg}} = \langle g|\, e\vec{r}\, |e\rangle \tag{2.14}$$

is the *transition dipole moment*.

A two-level atom interacting with light is described by the optical Bloch equations. A detailed description and derivation of these equations can be found in standard textbooks, e.g. [24]. In the scope of this theses, only a few applications of them will be important, which are listed in the following. The total *photon scattering rate* [25]

$$R_{\text{sc}} = \frac{\Gamma}{2}\frac{I/I_{\text{sat}}}{1 + I/I_{\text{sat}} + 4(\Delta/\Gamma)^2} \tag{2.15}$$

describes the rate at which photons are scattered by the atom. Scattering refers to the absorption of a photon by the atom and the subsequent spontaneous emission of a photon in a random direction. Here, $\Delta = \omega - \omega_0$ is the detuning of the light field from atomic resonance, $I = 1/2\, c\epsilon_0 E_0^2$ is the intensity of the light field and

$$I_{\text{sat}} = \frac{c\epsilon_0\Gamma^2\hbar^2}{4|\vec{\epsilon}\cdot\vec{d}_{\text{eg}}|^2} \tag{2.16}$$

is the *saturation intensity* of the transition [25]. The scattering rate has a Lorentzian frequency dependence with a full width at half maximum of $\Gamma\sqrt{1 + I/I\text{sat}} > \Gamma$. For this reason, the natural decay rate is also denoted as *natural linewidth*.

The on-resonance ($\omega = \omega_0$) scattering rate is linear in intensity for $I \ll I_{\text{sat}}$:

$$R_{\text{sc}} \overset{I \ll I_{\text{sat}}}{\approx} \frac{\Gamma}{2}\frac{I}{I_{\text{sat}}}. \tag{2.17}$$

For large intensities ($I \gg I_{\text{sat}}$), the on-resonance scattering rate saturates at

$$R_{\text{sc}} \overset{I \gg I_{\text{sat}}}{\approx} \frac{\Gamma}{2}. \tag{2.18}$$

At $I = I_{\text{sat}}$, the on-resonance scattering rate reaches half its maximum value.

The *scattering cross section* σ is a measure for the power radiated away due to scattering per unit of incident intensity, and from Eq. 2.15 becomes [25]

$$\sigma = \frac{\sigma_0}{1 + I/I_{\text{sat}} + 4(\Delta/\Gamma)^2}, \tag{2.19}$$

with the on-resonance cross section

$$\sigma_0 = \frac{\hbar\omega_0\Gamma}{2I_{\text{sat}}}, \tag{2.20}$$

which, using Eqs. 2.13 and 2.16 and $\lambda_0 = 2\pi\omega_0/c$, simplifies for the two-level atom to

$$\sigma_0 = \frac{3\lambda_0^2}{2\pi}. \tag{2.21}$$

Lambert-Beer law When a weak ($I \ll I_{\text{sat}}$) resonant beam of light travels a distance x through a medium of atoms with constant density n, the intensity of the beam is reduced due to photon scattering. The intensity as a function of distance is given by [24]

$$I(x) = I_0 \exp(-\sigma n x), \tag{2.22}$$

where I_0 is the initial intensity of the beam. This is known as the *Lambert-Beer law of absorption*. If the density is not constant, it must be integrated over the entire distance of interaction, modifying the equation to

$$I(x) = I_0 \exp\left(-\sigma \int_0^x dx' n(x')\right). \tag{2.23}$$

Doppler effect In the discussion above, we ignored the motion of the atoms. An atom moving with a velocity relative to the laboratory frame[3] sees a different frequency [24]

$$\omega' = \omega - k v_{\parallel} \tag{2.24}$$

due to the *Doppler effect*, where $k = \omega/c$ is the wavenumber of the light field in the laboratory frame and $v_{\parallel}$ is the velocity component of the atom parallel to the propagation direction of the light field. An atom moving in the direction of the light sees a lower frequency, while an atom moving counter to the direction of the light sees a higher frequency. The Doppler effect can be incorporated into the equations above by extending the detuning defined in Eq. 2.15 by the Doppler shift [24]:

$$\Delta = \omega - \omega_0 \rightarrow \Delta = \omega - (\omega_0 + k v_{||}). \tag{2.25}$$

Thus, the atomic resonance frequency, as observed in the laboratory frame, changes from ω_0 for a stationary atom to $\omega_0 + k v_{\parallel}$ for a moving atom. Therefore, the resonance frequency for an atom moving in the direction of the light field is increased (blue-shifted), while for an atom moving counter to the light field, it is decreased (red-shifted), as seen from the laboratory frame.

[3] The laboratory frame is defined as the frame in which the light field has the frequency ω, e.g. the frequency an observer standing in a laboratory would measure, hence the name

Alkali metals *Alkali metals* are atoms with a single valence electron and filled inner shells, giving them a hydrogen-like level structure. Their eigenstates are characterized by the quantum numbers N, L, S, J, I, F and m_F [24]. N is the principal quantum number, L ($L = 0,...,N-1$) is the orbital angular momentum quantum number and $S = 1/2$ is the spin quantum number. J is the total electron angular momentum resulting from the coupling of the spin and orbital angular momentum of the electron and can take the values $|L - 1/2|$ and $L + 1/2$. For the ground state with principal quantum number n and $L = 0$ the only possible value is $J = 1/2$. This state is usually labeled by the term symbol $n^2S_{1/2}$, where the superscript $2S + 1$ denotes the multiplicity, the letter S indicates the $L = 0$ state and the subscript gives the value of J. For the first excited state with the same principal quantum number and $L = 1$, there are two states with $J = 1/2$ and $J = 3/2$, corresponding to the term symbols $n^2P_{1/2}$ and $n^2P_{3/2}$, respectively. The energy of these states is shifted according to the value of J, resulting in a so-called *fine-structure doublet* for the transition $L = 0 \rightarrow L = 1$. The transition $n^2S_{1/2} \rightarrow n^2P_{1/2}$ is denoted as the D_1 line, while the transition $n^2S_{1/2} \rightarrow n^2P_{3/2}$ is denoted as the D_2 line.

Each of these transitions additionally exhibit *hyperfine structure* [24], which results from the coupling of the total electron angular momentum J with the nuclear spin I to form the total atomic angular momentum F. The quantum number F can take the values $|J - I| < F < J + I$. Each state is again shifted according to the value of F. For each F, there are $2F + 1$ degenerate substates labeled by the magnetic quantum number m_F, which takes values from $-F$ to F in integer steps. Angular momentum conservation during the absorption or emission of a photon restricts possible transitions between two states with different F and m_F to $\Delta F = 0, \pm 1$ and $\Delta m_F = 0, \pm 1$[4] [24].

Dipole moments for hyperfine transitions Consider the transitions between two hyperfine substates $|F\, m_F\rangle$ and $|F'\, m'_F\rangle$, where the primed variables refer to the excited state and the unprimed to the ground state. According to the Wigner-Eckhart theorem, the dipole matrix elements can be written as [25]

$$\langle F\, m_F|\, er_q\, |F'\, m'_F\rangle = \langle F||e\vec{r}||F'\rangle \langle F\, m_F|F'\, 1\, m_F\, q\rangle. \tag{2.26}$$

The first factor, $\langle F||e\vec{r}||F'\rangle$, is the reduced dipole matrix element, which does not depend on the m_F numbers anymore, while the second factor, $\langle F\, m_F|F'\, 1\, m_F\, q\rangle$, is the Clebsch-Gordan coefficient, which encodes the m_F dependence. The index q labels the component of $\vec{r}$ in a spherical basis, such that $q = -1$ an $q = +1$ correspond to circularly polarized light (σ^- and σ^+ transitions) and $q = 0$ to linearly polarized light (π transitions). The reduced matrix element can be further simplified by factoring out the F dependence into another reduced matrix element $\langle J||e\vec{r}||J'\rangle$ and a Clebsch-Gordan coefficient [25].

By exploiting the symmetries of the dipole operator, one can show that each excited hyperfine substate in a given line (D_1 or D_2) decays with the same rate [25]

$$\Gamma = \frac{\omega_0^3}{3\pi\epsilon_0\hbar c^3} \frac{2J+1}{2J'+1} \langle J||e\vec{r}||J'\rangle, \tag{2.27}$$

where the factor $(2J + 1)/(2J' + 1)$ is usually denoted as the degeneracy factor. The degeneracy factor is $1/2$ for the D_2 line and 1 for the D_1 line.

[4] An exception is $\Delta F = 0$ and $m_F = 0$, which is not allowed

For an isotropic light field with equal components in all three polarizations (σ^+, σ^-, π), that couples to a $F \rightarrow F'$ transition, the coupling is independent of the magnetic substate m_F. The atom can be treated as an effective two-level atom with dipole moment [25]

$$|\vec{d}|^2 = \frac{1}{3} S_{FF'} |\langle J||e\vec{r}||J'\rangle|^2. \tag{2.28}$$

The factor of $1/3$ reflects the fact that any polarization of the light field only interacts with one of the three components of the dipole moment. This situation is equivalent to a polarized light field interacting with unoriented atoms, i.e. where the population is randomly distributed among the m_F substates [24]. The values $S_{FF'}$ provide a measure for the relative strength of transitions between different F levels. These values obey the sum rule

$$\sum_{F'} S_{FF'} = 1, \tag{2.29}$$

independent of F. Substituting Eqs. 2.28 and 2.27 into the formula for the scattering cross section, Eq. 2.20, leads to an effective on-resonance cross section for $F \rightarrow F'$ transitions given by

$$\sigma_0^{(F\rightarrow F')} = \sigma_0 \cdot \frac{1}{3} \frac{2J'+1}{2J+1} S_{FF'}, \tag{2.30}$$

with the two-level on-resonance scattering cross section σ_0, Eq. 2.21.

2.3 The elements lithium and rubidium

This section provides a summary of the most important physical and optical properties and numbers of the alkali metals lithium (Li) and rubidium (Rb), particularly concerning the previously introduced quantities. Lithium comes in a fermionic isotope ^{6}Li with a natural abundance of 7.6 %, and a bosonic isotope ^{7}Li with a natural abundance of 92.4 % [26]. Rubidium comes in two stable bosonic isotopes, ^{85}Rb and ^{87}Rb, with relative natural abundances of 72.17 % and 27.83 %, respectively [25, 27]. In the following, only the fermionic isotope of Li and both isotopes of Rb will be considered.

Vapor pressure The vapor pressure p (in Pa) as a function of temperature T (in K) can be modelled by the equation [28]

$$\log_{10}(p) = 5.006 + A + \frac{B}{T}, \tag{2.31}$$

where A and B are constants that depend on the element and its phase. This equation provides only a rough estimate of the vapor pressure, with an accuracy of at least $\pm 5\,\%$[5]. The constants for the liquid and solid phase of Li and Rb, along with their melting point, are shown in Tab. 2.1. A plot of the vapor pressure as a function of temperature for both elements is shown in Fig. 2.4.

Optical properties The hyperfine structure of the D_2 line is of interest as it is used for the spectroscopy. The hyperfine structure of the isotopes ^{85}Rb, ^{87}Rb and ^{6}Li is shown schematically in Fig. 2.3. Both ^{85}Rb and ^{87}Rb have a half-integer nuclear spin I, which results in an integer total atomic angular momentum F, making both isotopes composite bosons. In contrast, ^{6}Li has an integer nuclear spin, classifying it as

[5] In the temperature range 25 °C $\leq T \leq$ 277 °C for Rb and 25 °C $\leq T \leq$ 727 °C for Li

a composite fermion. The values for the nuclear spin of these isotopes, along with the wavelength λ_0 of the D_2 transition and the natural decay rate Γ of the excited states, are listed in Tab. 2.2. Additionally, the smallest saturation intensity I_{sat} is shown[6].

Collisional properties As introduced in section 2.1, collisions can be modelled by van der Waals interactions, with the total collisional cross section introduced in Eq. 2.5. The C_6 coefficients for collisions involving Li and Rb were numerically calculated in [29] and are listed in Tab. 2.3.

Element	T_M [°C]	A_s	B_s	A_l	B_s
Li	180.5	5.667	−8310	5.055	−8023
Rb	39.3	4.857	−4215	4.312	−4040

TABLE 2.1: Melting point T_M and vapor pressure constants A and B (see Eq. 2.31) for Li and Rb, where the subscript of A and B indicate the phase in which the element is present (s=solid, l=liquid). The values for A and B are taken from [28] and the values for T_M from [26, 27].

Isotope	λ_0 [nm]	$\Gamma/2\pi$ [MHz]	I_{sat} [mW/cm^2]	I
^{85}Rb	780.2	6.067	1.67	5/2
^{87}Rb	780.2	6.065	1.67	3/2
^{6}Li	671.0	5.872	2.54	1

TABLE 2.2: D2 line transition wavelength λ_0, corresponding excited state natural decay rate Γ, representative saturation intensity I_{sat} and nuclear spin quantum number I for the three isotopes ^{85}Rb, ^{87}Rb and ^{6}Li. Values are taken from [25–27].

Atom pair	C_6 [au]
Rb - Rb	4690
Li - Li	1389
Rb - Li	2545

TABLE 2.3: C_6 coefficients in atomic units (au) for van der Waals interactions between two Rb atoms, two Li atoms and one Rb atom with one Li atom, respectively.

[6] Since the saturation intensity depends on the polarization of the light and the atomic alignment (see Eq. 2.16), the smallest value, corresponding to the cyclic cooling transition [25], is often quoted as a representative value

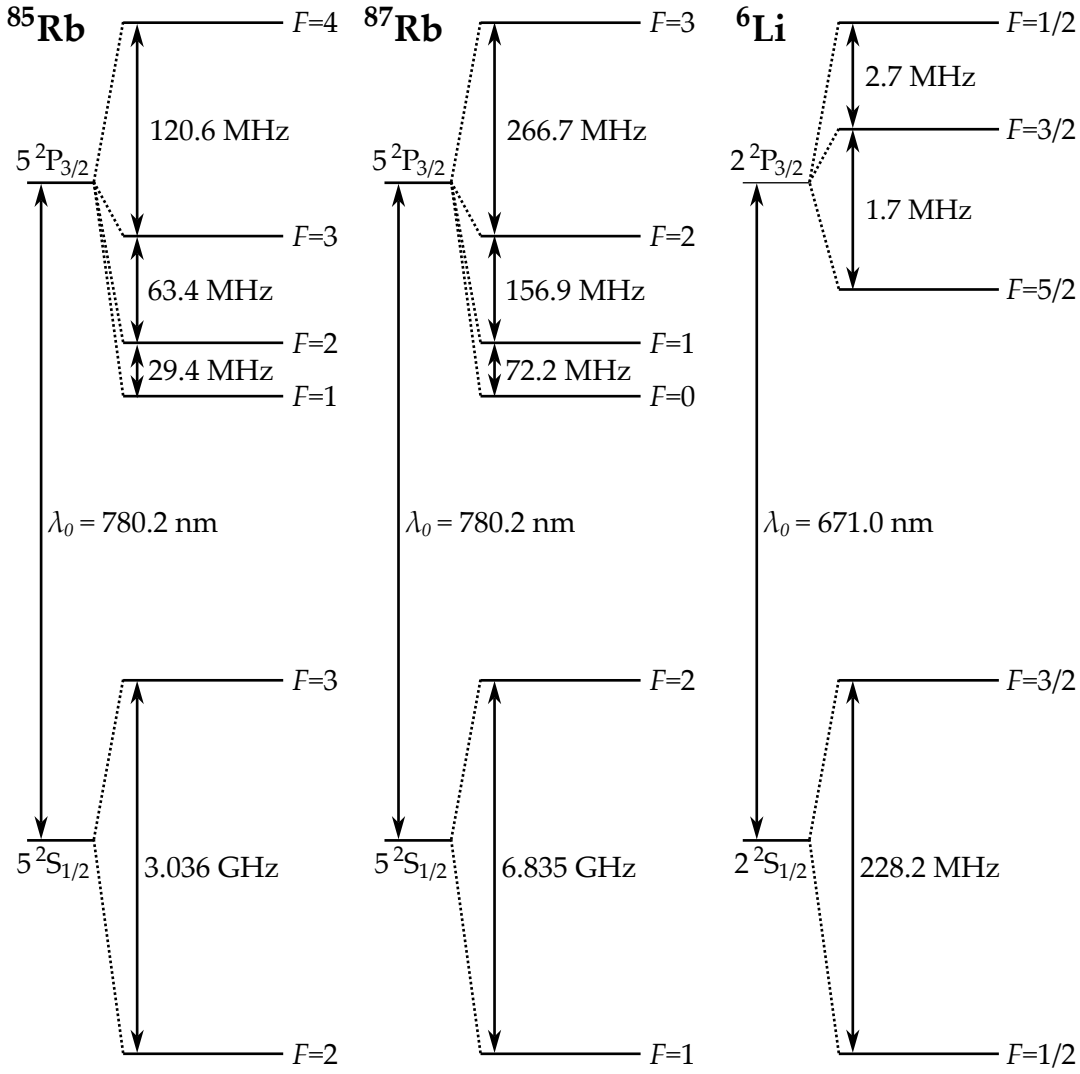

FIGURE 2.3: Hyperfine structure with frequency splittings of the D2 line transition ($^2S_{1/2} \rightarrow {}^2P_{3/2}$) with wavelength λ_0 for ^{85}Rb, ^{87}Rb and ^{6}Li. The splittings are not to scale. Values are taken from [25–27].

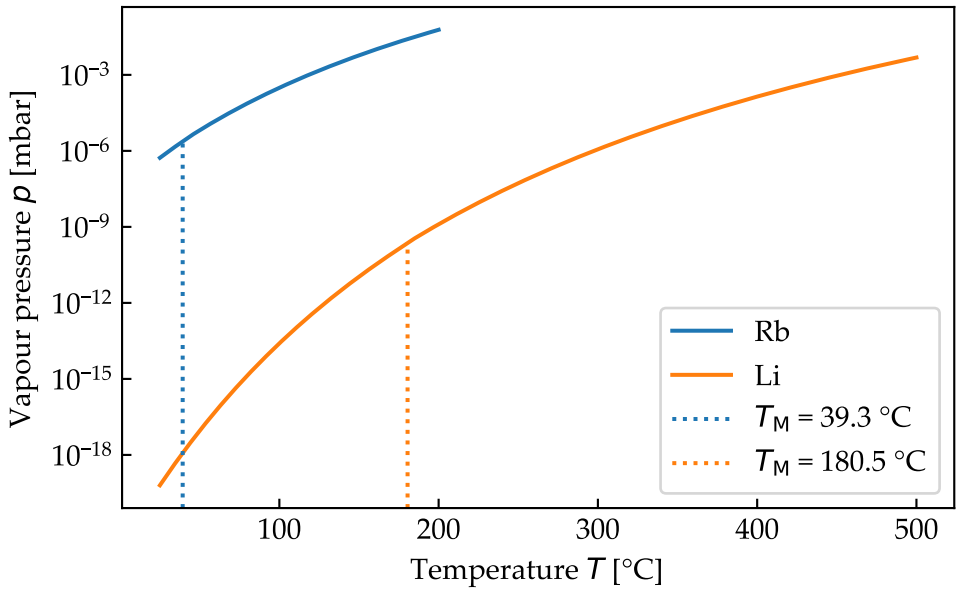

FIGURE 2.4: Vapor pressure p of lithium and rubidium as a function of temperature T calculated using Eq. 2.31 and Tab. 2.1. The dashed lines indicate the melting points T_M of each element.

Chapter 3

Source Design and Construction

In this chapter, the design of the dual-species atomic beam source as well as its experimental realization is described. Within the scope of this theses, the source was built as a stand-alone test setup and not yet as the final source.

The source is inspired by the design of the Stamper-Kurn group [15], where a common Zeeman slower is fed by a source that generates an overlapping beam of Li and Rb. In their source, the beam effuses from a common mixing chamber [30] fed by two individual reservoirs for Li and Rb. A single-reservoir design is not possible due to the large difference in vapor pressure between the two elements, as seen in Fig. 2.4. In their setup, particular considerations must be made to prevent backflow from the mixing chamber into the reservoirs as well as to account for chemical reactions between Rb with Li [30]. To simplify these considerations, some modifications were made with respect to their source. Specifically, instead of using a mixing chamber, two separate effusive sources, connected in a kind of series connection, are used.

In section 3.1, the working principle of the dual-species source is described, followed by its experimental implementation in section 3.2. Then, in section 3.3, the process of cleaning the alkali metals, filling them into the setup and the subsequent bakeout of the vacuum system is described. Finally, in section 3.4, some peculiarities regarding the reaction of Li with glass are discussed.

3.1 Source design

The dual-species atomic beam source consists of two separate reservoirs for Li and Rb, separated by a middle section with an adjustable shutter (see Fig. 3.1). The oven is designed to allow for either single-species operation of both elements independently of each other or for combined dual-species operation. The working principle of these three modes of operation is described below.

Rb-only operation During the single-species operation of Rb, the Rb reservoir is heated to $100\,^{\circ}\mathrm{C} - 120\,^{\circ}\mathrm{C}$, while the rest of the setup is kept at room temperature. In this temperature range, the vapor pressure of $3 \cdot 10^{-4}\,\mathrm{mbar} - 1 \cdot 10^{-3}\,\mathrm{mbar}$ (see Eq. 2.31) allows for the generation of an atomic beam with sufficiently high flux on the order of $10^{15}\ \mathrm{s}^{-1}$, while simultaneously maintaining a reasonable reservoir lifetime of several thousand hours. The mean free path is calculated to be in the range of $6\,\mathrm{mm} - 1.9\,\mathrm{mm}$ using Eqs. 2.6, 2.5 and 2.1.

Rb atoms effuse in the molecular flow regime through a circular orifice with a length of 1 mm and a diameter of 2 mm into the middle section. The orifice is extended by a cylinder with a length of 16 mm and a diameter of 14 mm. This nozzle design is adopted from the current ion microscope experiment [17]. The shutter in the middle section is opened, ensuring the direct path between the Rb nozzle and

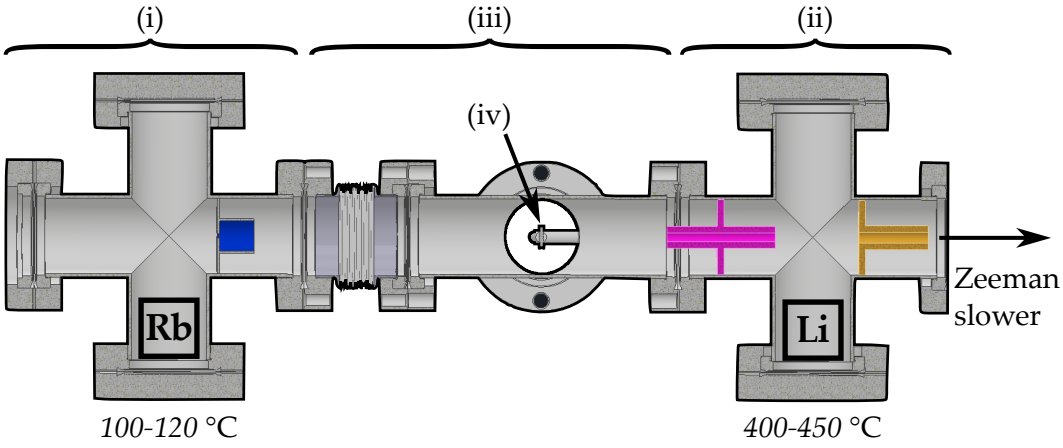

FIGURE 3.1: Schematic sketch of the dual-species source. The source is divided into three sections: the Rb reservoir (i), the Li reservoir (ii) and a middle section (iii) separating both reservoirs. Rb atoms effuse out of an orifice with a diameter of 2 mm and a thickness of 1 mm, which is surrounded by a cylinder that is 14 mm wide and 16 mm long (blue). They enter the Li reservoir through an intermediate nozzle (pink) with a length of 50 mm and a diameter of 4 mm, before exiting the reservoir together with the Li atoms through a 32 mm long and 5 mm wide exit nozzle (yellow) to form an overlapping atomic beam propagating towards a common Zeeman slower. There is an additional shutter (iv) that can move up and down to block or open the direct path between the Rb nozzle and the intermediate nozzle. Details about the working principle are described in the text.

the intermediate nozzle of the Li reservoir is not blocked. The intermediate nozzle has a length of 50 mm and a diameter of 4 mm. As the Rb atoms propagate through the middle section, the beam expands, and a small fraction of atoms is cut out by the intermediate nozzle. Due to the low vapor pressure of Li at room temperature, these atoms propagate through the Li reservoir unaffected and exit through the 32 mm long and 5 mm wide exit nozzle towards the Zeeman slower as a collimated beam. Most atoms stick to the walls in the middle section. Later it will turn out that these atoms have a greater significance than originally expected, more on this in chapter 4. The intermediate nozzle design prevents large amounts of Rb from entering the Li reservoir, thus avoiding chemical reactions and solution formation within the Li reservoir.

During the Rb-only operation, the Li reservoir can, in principle, be heated to a similar temperature as the Rb reservoir to prevent clogging in the intermediate and exit nozzles. At this temperature, the vapor pressure of Li remains small enough to not interfere with the Rb atoms. However, as described next, during the Li-only operation, the Li reservoir is heated to a much higher temperature, therby effectively cleaning the nozzles of any Rb. Therefore, the necessity of heating the Li reservoir during Rb-only operation depends on how, and for how long, the different operation modes are carried out in a real experiment.

Li-only operation The Rb reservoir is kept at room temperature and the Li reservoir is heated to 400 °C − 450 °C, such that the vapor pressure is on the order of

$1 \cdot 10^{-4}$ mbar $- 1 \cdot 10^{-3}$ mbar to ensure similar numbers for the total flux and reservoir lifetime as for Rb. The mean free path is in the range of 78 mm $-$ 13 mm, keeping the source in the molecular flow regime. A fraction of Li atoms effuses from the oven through the exit nozzle towards the Zeeman slower, where the beam divergence is determined by the dimensions of the exit nozzle, as discussed in section 2.1.

Additionally, Li atoms effuse through the intermediate nozzle into the middle section. To minimize negative effects on the reservoir lifetime, the intermediate nozzle is longer and narrower than the exit nozzle, thereby reducing the total flux effusing through it (see Eq. 2.11), while still allowing sufficient amount of Rb atoms to pass through during Rb-only operation. The back-flowing Li beam would hit the Rb nozzle, leading to its clogging over time due to the lower operating temperature compared to the Li reservoir, as well as to potential chemical reaction between Li and Rb within the Rb reservoir. To prevent this, the shutter in the middle section can be closed to block the Li atoms from reaching the Rb nozzle.

Dual-species operation In dual-species operation, both reservoirs are heated, resulting in an overlapping beam of Li and Rb atoms after the exit nozzle. The shutter must be opened, but collisions between the back-flowing Li atoms and the Rb beam prevent Li atoms from reaching the Rb nozzle. For this to work, it is important that the Rb nozzle operates near the limit between the molecular flow and continuum flow regime [30].

When analyzing the flux of Rb atoms through the exit nozzle as a function of Li reservoir temperature, a decrease in flux is expected with increasing temperature due to the rising collision rate between the Rb beam and the Li atoms. This reduction is expected around a temperature on the order of 400 °C, considering the previously calculated mean free path in the Li reservoir[1] and the dimensions of the reservoir. This, along with considerations regarding clogging, is another reason why the Li reservoir is placed in front of the Rb reservoir: Due to the smaller mean free path in a Rb vapor (a factor of 10 less compared to a Li vapor), the Li atoms would not be able to pass through the Rb reservoir under the specified conditions, making a dual-species operation impossible.

Since only a small fraction of Rb atoms enter the Li reservoir relative to the total flux, the total Li flux is expected to remain unaffected by the Rb beam. The main goal of this theses is to experimentally test these two scenarios - specifically, how the Li and Rb beams influence each other during dual-species operation.

3.2 Vacuum system

The experimental implementation of the source can be seen in Fig. 3.2. To maintain a continuous atomic beam, ultrahigh vacuum (UHV) conditions are required to avoid collisions with background gases. The vacuum system is constructed from standard stainless steel components[2] of grade 304L with DN35CF-DN40CF conflat (CF) flange connections. The connections are sealed with gold-plated oxygen-free

[1] The mean free path of an Li atom in a Li vapor is of course different that of a Rb atom in a Li vapor due to differing scattering cross sections. However, since the C_6 coefficient for Li-Li and Rb-Li collisions are on the same order (Tab. 2.3), and the collisional cross section only depends on $C_6^{2/5}$ (Eq. 2.5), the mean free path will also be on the same order

[2] Kurt J. Lesker: F0275X000N, T-0275, C-0275, C6-0275

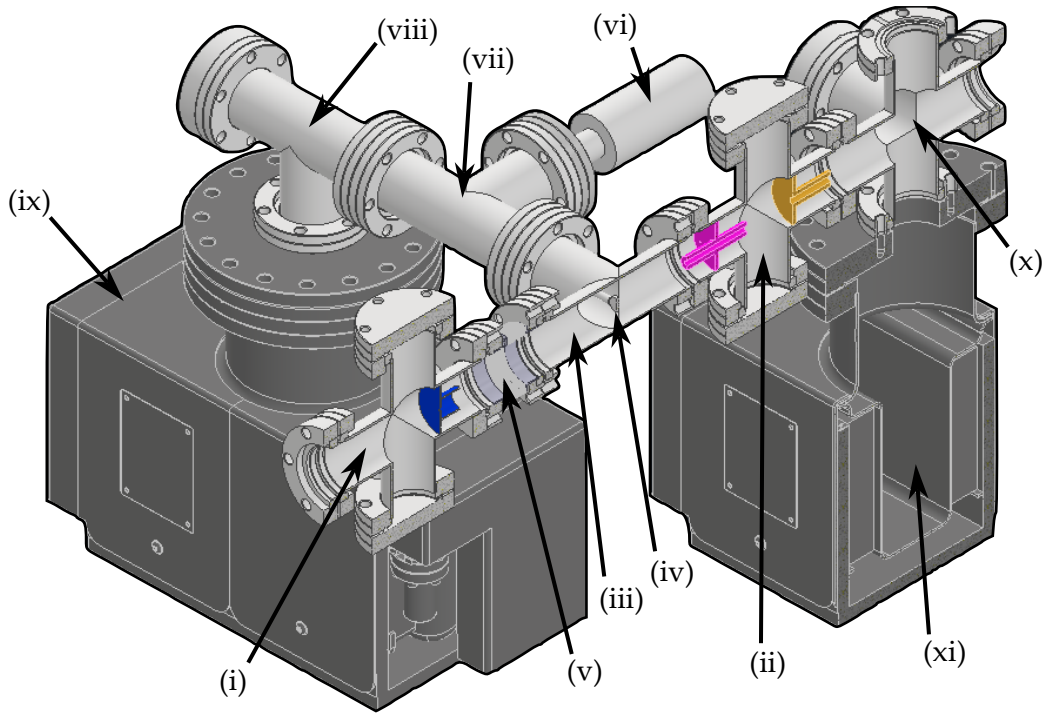

FIGURE 3.2: Experimental setup of the dual-species source. Shown in the front is the Rb reservoir (i), the middle section and the Li reservoir (ii), as described in Fig. 3.1. The middle section consist of a 4-way cross (iii) containing the shutter (iv) and a viewport in the front (not shown because of sectional view), along with a flexible bellow (v) allowing for the alignment of the Rb nozzle (blue) with the two nozzles in the Li reservoir (pink and yellow). The shutter is controlled mechanically by a rotatory feedthrough (vi), connected via a T-cross (vii). Another T-cross (viii) is attached, with a viewport at the back and an ion pump connected from below (ix). An additional 6-way cross (x) is connected to the Li reservoir, providing optical access in this section with viewports attached on the sides. At the bottom of the 6-way cross, another ion pump (xi) is attached and at the top sits a valve (not shown), which is connected to a turbo pump to pump down the system.

high-conductivity (OFHC) copper gaskets[3], except for the four gaskets in direct contact with the Li reservoir, where annealed nickel gaskets[4] are used because hot Li corrodes copper [16]. The three nozzles are custom-made in the in-house mechanics workshop and welded vacuum tight into the 4-way crosses, see [31] for detailed information on the fabrication process.

The setup can be divided into four regions: the Rb reservoir, the middle section and the Li reservoir, as explained in the previous section, and an additional 6-way cross beyond the Li reservoir. Viewports attached to the sides of the 6-way cross allow for optical access to the system, which will later be used for performing spectroscopy on the atomic beam. An ion pump[5] is connected at the bottom of the cross to maintain the vacuum during the measurements. At the top of the cross is an additional valve (not shown in the figure) which is connected to an integrated pump

[3]Kurt J. Lesker: GA-0275LBG
[4]Kurt J. Lesker: GA-0275NIA
[5]Agilent: VacIon Plus 40 Pump

system[6] containing a rotary vane pump and a turbo pump, used for the initial pump down of the vacuum system. The Rb reservoir is connected to the middle section via a bellow[7] that allows the Rb nozzle to be aligned with the two Li nozzles by using the viewport at the front of the 6-way cross and an additional viewport at the back of the Rb reservoir. The shutter, also custom made in the in-house mechanics workshop, can be mechanically raised or lowered using a rotatory feedthrough[8]. Another ion pump is connected to the middle section to maintain the vacuum conditions, particularly for removing Rb that accumulates during the source operation. Additional viewports are attached to the front and back of the middle section to ensure optical access. All viewports in the setup are made of annealed kodial glass[9].

Both reservoirs are independently heated from the outside using low-voltage heating cables[10] powered by a power supply[11], which is regulated by a temperature controller[12]. The temperature is measured externally using thermocouples[13], with two thermocouples attached to each reservoir at different locations to monitor the temperature at both the source material and the nozzles independently. The nozzles should ideally be maintained at a slightly higher temperature than the reservoir to avoid clogging [15]. This can be achieved by wrapping more heating cable around the nozzle and adding additional isolation.

Before filling the system with Li and Rb, it is pumped down using the turbo pump and baked at approximately 180 °C for 10 days. The ion pumps are switched off during the bakeout. The bellow is kept at a lower temperature, as it is only rated up to 80 °C, which limits the final pressure. Once the system cools down, it reaches a final pressure of $7.5 \cdot 10^{-9}$ mbar, which is sufficient for the intended purpose.

3.3 Source filling and bakeout

After the system is baked, the alkali metals are placed in their respective reservoir. Both Li and Rb are highly reactive with water and air, so they must be stored and handled carefully to prevent oxidation. Rb is typically supplied as solid material in an evacuated glass ampoule[14], while Li comes in small chunks stored in mineral oil. Because the natural abundance of ^{6}Li is quit low, enriched ^{6}Li chunks with a purity of 95 % are used[15]. Rb is used in its natural isotopic composition.

Before placing the Li chunks in the vacuum system, they have to be cleaned to remove oil contamination. The chunks are first placed in a clean beaker filled with cyclohexane. After a few minutes, they are taken out and the top oxidation layer is cut away with a knife. The chunks are then placed back into a fresh beaker with cyclohexane. This cleaning process is repeated three to four times to ensure that most of the oil contamination is removed. The Rb material, beeing 99.75 % pure and vacuum sealed, does not require a cleaning procedure.

Once the Li chunks are mostly oil-free, both Li and Rb can be placed into the system. The vacuum system is filled with high-purity argon to prevent oxidation.

[6] Pfeiffer Vacuum: HiCube300
[7] Vacom: EWB40R-10
[8] Agilent: L6691301
[9] Kurt J. Lesker: VPZL-275
[10] Horst: HSQ0122-160W-16V-900°C, HS010-110W-16V-450°C
[11] EA Elektro-Automatik EA-PS 3016-20 B
[12] Jumo: diraTRON (Typ 702110/8-0300-23/000)
[13] RS Components: 334-2622, 621-2271
[14] Thermo Scientific Chemicals: 010315
[15] Sigma Aldrich: 340421

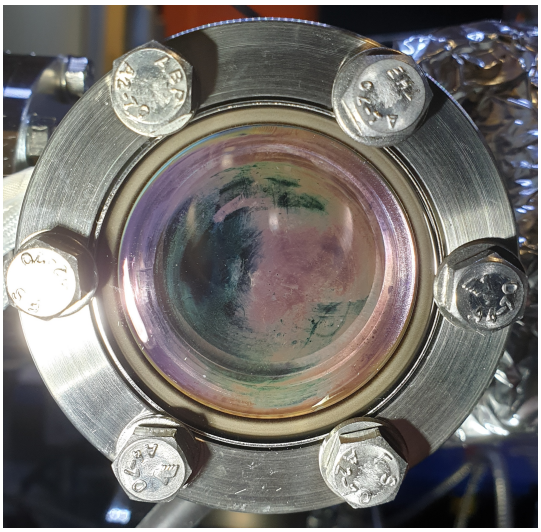

FIGURE 3.3: Picture of the viewport in the middle section after a few hours of baking the Li reservoir at 450 °C. The viewport was not isolated, acting as a cold spot during the bakeout process. Purple depositions were observed, which are likely due to mineral oil released from the Li chunks. These depositions can be removed from the system by heating the viewport and using the turbo pump to pump out the released oil.

The Li chunks are placed into their reservoir, while the Rb ampule is cracked open and wiped with isopropanol before being inserted into its reservoir. To minimize oxidation, the exposure to air is kept as short as possible. Afterwards, the system is closed and the argon atmosphere is pumped out using the turbo pump.

Next, the system is baked again to remove any residual oil contaminations that may have remained inside the Li chunks. This process is still performed with the turbo pump, while the ion pumps remain off. The entire system is first heated to approximately 120 °C, after which the Li reservoir temperature is slowly increased to 450 °C. During this process, the pressure and composition of the residual gas is monitored using a quadrupole mass spectrometer[16] to detect possible signatures of mineral oil in the system [32]. A pressure spike was observed around 280 °C, indicating the release of residual oil contamination from the Li chunks. After this spike, the pressure followed the expected temperature increase again.

Initially, the viewport in the middle section was not isolated, so it acted as a cold spot during baking. A picture of this viewport, taken after several hours of baking, is shown in Fig. 3.3. Purple depositions, attributed to mineral oil, are visible. However, the oil residues can be evaporated by also heating the viewport. After a total of one day of baking, the pressure went down again. The Rb reservoir is shortly heated to 150 °C for around three hours to remove any residual oxidation layer. Afterwards, the system can cool down. Once the system reaches room temperature, the ion pumps are switched on and the valve to the turbo pump is closed. After another day, the pressure in the system, as shown by the ion pumps, stabilized in the range of $10^{-10} - 10^{-9}$ mbar.

The source is now ready for spectroscopic measurements. Before discussing these measurements, it is important to highlight one additional consideration when working with Li: its chemical reactivity with glass.

[16] Stanford Research Systems: RGA100

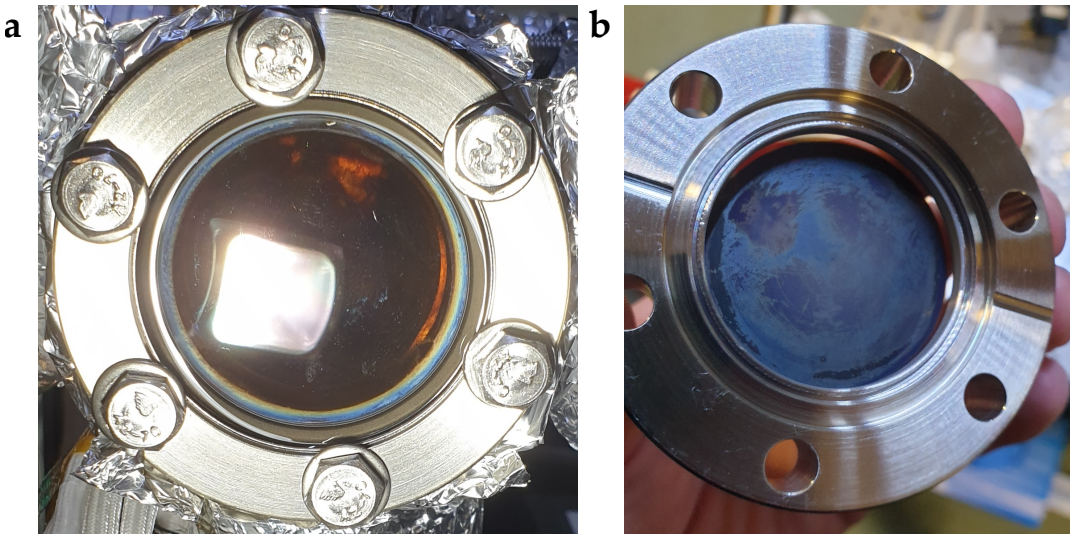

FIGURE 3.4: **a** Picture of the viewport in direct contact with the Li beam after 20 hours of Li operation at 450 °C. A chemical reaction between Li and the glass results in a coating on the window that reduces its transmission. The bright white spot visible on the viewport is the reflection of a flashlight. At this point, the transmission of light with wavelength 671 nm has decreased to around 25 %. **b** The same viewport after two months of operation. A black layer formed on the surface, reducing its transmission to nearly zero.

3.4 Reaction of lithium with glass

The observations described in this section were made during the spectroscopic measurements, unlike the preparations discussed in the previous sections. However, they are included in this chapter due to their relevance in the design of a real experimental setup beyond a mere test setup.

When dealing with Li, further precautions must be taken for viewports that come in direct contact with Li. While Rb mostly forms a layer on glass without corroding it, Li reacts strongly with the glass, causing irreversible damage. A picture of the viewport at the 6-way cross, which is in direct contact with the Li beam, is shown in Fig. 3.4a. The picture was taken after around 20 hours of Li operation at 450 °C. The viewport was not heated during the operation. A black layer forms on the glass surface, reducing the transmission. At this point, the transmission of light at 671 nm dropped to about 25 %. Using the theoretical flux from Eq. 2.11 and the expected beam divergence, as well as the geometry of the setup, the estimated number of Li atoms on the viewport is around 10^{15} atoms per second, corresponding to $7 \cdot 10^{19}$ atoms after the full 20 hours. Such a coating can no longer be removed by simply heating the window. However, some groups report that illuminating the viewport with broadband UV light can break down the layer[17], though this has not been tested in this setup.

After about two months of operation, the transmission of the viewport dropped to nearly zero, and it was replaced by a new one. A picture of the inside of the old viewport is shown in Fig. 3.4b. It is reported that heating the viewport during or shortly after Li operation can minimize corrosion [16]. This was tested with the

[17] Private communication: Group of Hecker Denschlag, University of Ulm

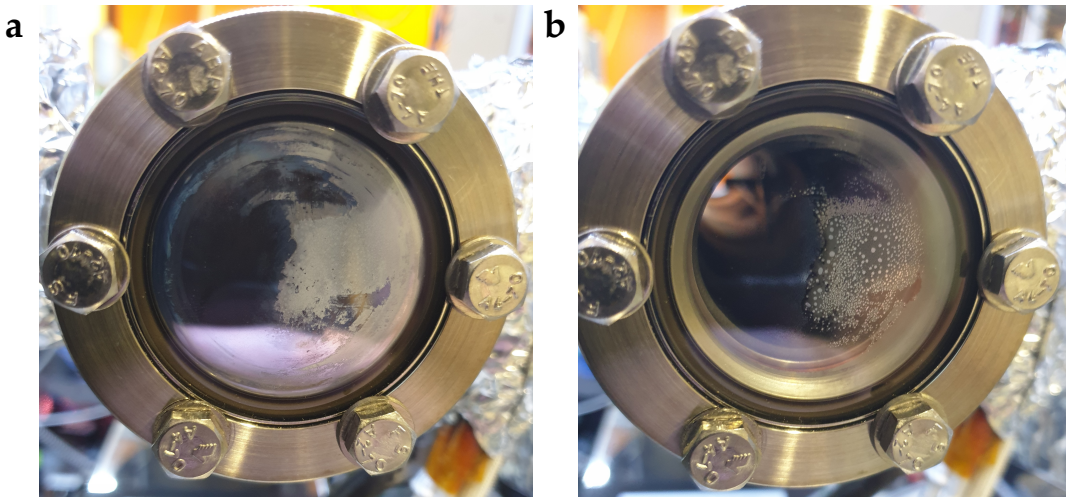

FIGURE 3.5: Effect of heating on viewport corrosion. **a** The viewport in the middle section after dual-species operation. Although not directly in contact with the Li beam, scattered Li atoms from collisions between the Li and Rb beams have coated the viewport. The white layer visible on the right is Rb deposition from previous Rb-only operation and is unrelated to the dual-species operation. **b** The same viewport after heating it to approximately 100 °C. Both the Li coating and most of the Rb deposition disappear. However, this process is only effective for Li if the coating is not too thick, and if heating is done before significant corrosion begins.

new viewport by heating it to approximately 100 °C[18], but only slight improvements were observed, likely because the incident flux of Li atoms was too high.

Heating was also tested on viewports that are not in direct contact with the Li beam, but instead are exposed to Li atoms through diffusive scattering. An example of this can be seen on the viewport in the middle section after dual-species operation, shown in Fig. 3.5. In Fig. 3.5a, the viewport is shown after dual-species operation without heating it. The viewport again shows a black coating on the left side, a result of Li atoms scattered from the Rb beam. The white deposition on the right is from previous Rb-only operation and is not related to the dual-species operation (more on the role of Rb in the middle section in chapter 4). The fact that they are uneven is probably due to a small temperature gradient caused by the hot Rb reservoir, which sits on the left in the picture. In Fig. 3.5b, the viewport is shown after it was heated to approximately 100 °C directly after dual-species operation. The black coating disappeared and transmission was restored. Additionally, most of the old Rb deposits were removed, leaving only small leftovers.

It is therefore important for the design of an experiment to protect the viewports that come into contact with Li. As it was shown, simple heating can be an effective solution, provided the number of incident Li atoms is not too high. Whether this works over long periods remains to be figured out in a long time test. This becomes especially important for the viewport through which the Zeeman slower light is introduced into the experiment, as it is directly exposed to the unslowed portion of the atomic beam. Apart from heating this viewport, using a metallic in-vacuum mirror can serve as an alternative solution to protect the window [15].

[18]The viewport was heated by wrapping a heating cable around the steel mount holding the window. The temperature was measured using a thermocouple held carefully against the glass, though the actual temperature may vary due to the lower thermal conductivity of glass

Chapter 4

Atomic Beam Characterization

In this chapter, the results of the spectroscopy of the atomic beams are presented. Before considering the overlapping beam of both elements, it first must be verified that the source works as expected in single-species operations for both atoms. In section 4.1, the measurement setup for the spectroscopic characterization of the atomic beams is shown. Section 4.2 describes how the total atomic beam flux is calculated from the recorded spectra. In sections 4.3 and 4.4, the results of the spectroscopy for Li and Rb in single-species operation are presented. As a preview, the Rb beam does not perform as expected, which necessitates modifications to the original source design. These changes are described in section 4.4.2, together with the spectroscopy of the Rb beam with the new design. Finally, section 4.5 discusses the results of the dual-species operation.

4.1 Measurement setup

The optical setup for the characterization the atomic beams is shown in Fig. 4.1. The vacuum system is shown in a half section, viewed from the top. A 780 nm light beam is generated by an external-cavity diode laser[1] (ECDL) and injected into a tapered amplifier system[2]. A 671 nm light beam is produced by second-harmonic generation of a Raman-amplified[3][4] ECDL with a wavelength of 1342 nm. The 671 nm and 780 nm beams are resonant to the D_2 line of Li and Rb, respectively. The wavelength of the light can be tuned across the entire D_2 line by rotating the diffraction grating in the ECDL [33], which is achieved via an electronically controlled[5] piezoelectric actuator. A full spectrum is measured by sweeping the light frequency and monitoring the absorption signal on an oscilloscope. To convert the time information into a frequency information, a reference signal with a known frequency spacing is recorded simultaneously. For the 780 nm light, a saturation spectroscopy signal is measured through a Rb vapor cell [34], while the 671 nm light is monitored using an ultra-low expansion cavity[6], functioning as a Fabry-Pérot interferometer with a free spectral range of 1.5 GHz [34].

The spectroscopy light is horizontally polarized, and its optical power is adjusted using a combination of a half-wave plate and a polarizing beamsplitter. A dichroic mirror is used to overlap the two beams, and a beamsplitter reflects a portion of the light onto a photodiode, which measures the light intensity without absorption for reference. A telescope composed of two lenses, with a magnification of six, can be

[1] Toptica Photonics: DL Pro
[2] Toptica Photonics: TA Pro
[3] MPB Communications: VRFA-SF
[4] Toptica Photonics: DL Pro
[5] Toptica Photonics: DLC pro
[6] Stable Laser systems

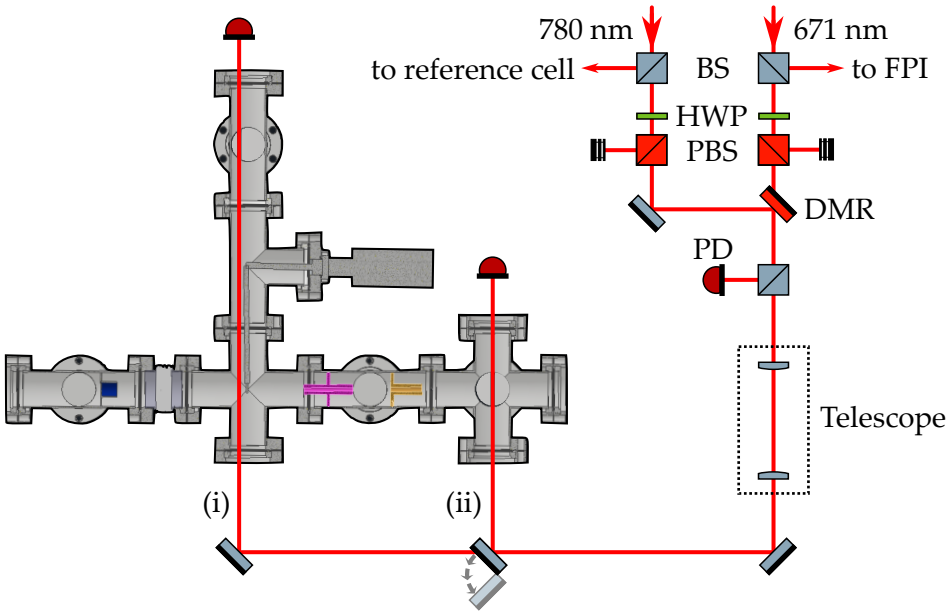

FIGURE 4.1: Measurement setup for the spectroscopic characterization of the atomic beam. The 780 nm and 671 nm light beams are first split into a spectroscopy beam and a reference beam using a beamsplitter (BS). The reference beam serves as a frequency reference, as described in the text. A saturation spectroscopy signal from a Rb reference cell serves as the reference for the Rb spectrum at 780 nm, while the Li spectrum at 671 nm is referenced to a Fabry-Pérot interferometer. A combination of a half-wave plate (HWP) and a polarizing beamsplitter (PBS) is used to horizontally polarize each beam and adjust its optical power. Both beams are overlapped on a dichroic mirror (DMR). A 50:50 beamsplitter is used to measure the intensity of the light without absorption using a photodiode (PD). An additional telescope, consisting of two lenses with sixfold magnification, can be moved in and out of the beam path. Using flip mirrors, the beam can be directed along two different paths for transversal absorption in the middle section (i) and in the 6-way cross (ii). All signals are measured with photodiodes and monitored with an oscilloscope.

positioned in or out of the beam path. Using flip mirrors, the beam can be directed along two different paths: transverse to the atomic beam in the middle section (i) or in the 6-way cross (ii). These paths are used for transversal absorption spectroscopy of the atomic beams to determine the flux and beam divergence. The absorption signals are measured with a photodiode.

4.2 Calculation of the flux

The flux of the atomic beam can be calculated using the Lambert-Beer law introduced in section 2.2. To do this, consider an infinitesimal light beam with area $dx\,dz$ and intensity $I_0 \ll I_{\text{sat}}$, which propagates in the y direction and intersects the atomic beam perpendicularly at a distance x from to the center of the atomic beam. The atomic beam propagates in z direction, where $z = 0$ corresponds to the orifice plane. The light beam has been attenuated to intensity I after penetrating the atomic beam. Fig. 4.2a shows a schematic sketch of the setup.

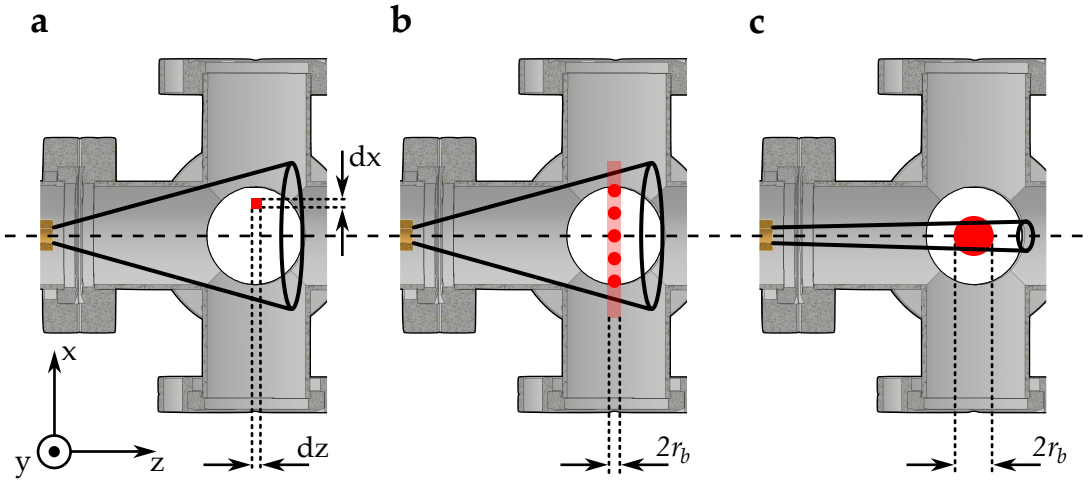

FIGURE 4.2: Sketch of the transversal absorption spectroscopy used for the calculation of the flux. **a** Shown is the 6-way cross after the Li reservoir, where the beam effuses from the exit nozzle (yellow) in z direction, with $z = 0$ set at the orifice plane. The vacuum tube clips parts of the atomic beam, as indicated by the solid black lines. An infinitesimal light beam (red) with area $dx\,dz$ is intersecting the atomic beam perpendicularly at a distance x relative to the centerline of the atomic beam. The infinitesimal flux through the interaction volume of the atomic and the light beam is given by Eq. 4.5, as discussed in the text. **b** A real Gaussian light beam with $1/e^2$ radius $r_\mathbf{b}$ intersects a divergent atomic beam, e.g., the Li beam effusing from the exit nozzle. If the spatial extension of the atomic beam is large compared to the light beam, the density can be assumed constant over the entire area of the light beam. The total flux, given by Eq. 4.15, is approximated by the integration over the red shaded area by measuring the flux through the small light beams at different distances x. **c** If the beam is collimated, e.g, the Rb beam due to collimation through the intermediate and exit nozzle, the total flux can be measured with a light beam whose radius equals the atomic beam size, leading to Eq. 4.16.

Resonant two-level atom For simplicity, first consider a two-level atom and resonant excitation, neglecting the Doppler effect. The influence of the Doppler effect and the hyperfine structure of Li and Rb will be added afterwards. Under these assumptions, Eq. 2.23 applies, which can be rewritten as

$$\ln\left(\frac{I_0}{I}\right)(x,z) = \sigma_0 \int dy\, n(x,y,z) \equiv D(x,z), \tag{4.1}$$

where $D = \ln(10)\,OD \approx 2.3 \cdot OD$, with OD being the *Optical density*. For convenience, D will be referred to as the optical density in the following. Here, $n(x,y,z)$ is the density profile across the atomic beam. The integral in Eq. 4.1 can be written as the product of a mean density $\bar{n}$ and an effective beam diameter $\bar{y}$:

$$\int dy\, n(x,y,z) = \bar{n}(x,z)\,\bar{y}(x,z). \tag{4.2}$$

These quantities are not independently determined, but their product $\bar{n}_{2d} = \bar{n}\bar{y}$ is given by Eq. 4.1 via,

$$\bar{n}_{2d}(x,z) = \frac{D(x,z)}{\sigma_0}, \tag{4.3}$$

where $\bar{n}_{2d}$ is the mean column density. The instantaneous total number of atoms dN in the interaction volume of the atomic and the light beam is given by multiplying the mean column density with the area of the light beam:

$$dN(x,z) = \bar{n}_{2d}(x,z)\, dx\, dz. \tag{4.4}$$

The average forward velocity is given by $\bar{v}\cos(\theta)$, where θ is the angle between the atoms trajectory and the atomic beam centerline, and $\bar{v}$ is the total average velocity. Due to the constraints of the vacuum system, the beam is probed only at small angles. Thus, the average forward velocity approximates to $\bar{v}$, and the time-of-flight for all probed angles θ is approximately $dz/\bar{v}$. Therefore, the flux $d\phi$ is given by

$$d\phi(x,z) = dN(x,z) \cdot \frac{\bar{v}}{dz} = \bar{n}_{2d}(x,z)\, \bar{v}\, dx. \tag{4.5}$$

Doppler effect Due to the Doppler effect, a light beam with fixed frequency $\omega = 2\pi f$ interacts only with a certain transverse velocity class of the atomic beam, given by Eq. 2.25. Therefore, Eq. 4.1 has an additional frequency dependence. The total mean column density, Eq. 4.3, is given by integrating the optical density over all velocity classes or, equivalently, all frequencies, normalized by the spectrally integrated scattering cross section, Eq. 2.19 [35]:

$$\bar{n}_{2d}(x,z) = \frac{\int df\, D(x,z,f)}{\int df \frac{\sigma_0}{1+4(2\pi f/\Gamma)^2}} = \frac{4}{\sigma_0\Gamma}\int df\, D(x,z,f) \tag{4.6}$$

.

D_2 line transition The integrated optical density over the entire D_2-line of Li or Rb is the sum of all allowed hyperfine transitions:

$$\frac{4}{\Gamma}\int df\, D(f) \overset{4.6}{=} \sum_F \sum_{F'} \sigma_0^{(F\to F')} \bar{n}_{2d}^{(F)}, \tag{4.7}$$

where the fact that each excited state has the same decay rate Γ was used (see Eq. 2.27). $n_{2d}^{(F)}$ is the mean column density of atoms in the ground state level with quantum number F. Since the atoms in the atomic beam are randomly oriented, Eq. 2.30 applies for the scattering cross section $\sigma_0^{(F\to F')}$. With that, Eq. 4.7 can be rewritten as

$$\frac{4}{\Gamma}\int df\, D(f) = \sum_F \sum_{F'} \left(\sigma_0 \cdot \frac{1}{3}\frac{2J'+1}{2J+1} S_{FF'}\right) \bar{n}_{2d}^{(F)} \overset{2.29}{=} \sigma_0 \cdot \frac{1}{3}\frac{2J'+1}{2J+1} \sum_F \bar{n}_{2d}^{(F)}, \tag{4.8}$$

where the fact that the relative hyperfine transition strengths $S_{FF'}$ obey the sum rule Eq. 2.29 was used. Given that all the atoms are distributed among the ground states, the sum over $\bar{n}_{2d}^{(F)}$ gives the total mean column density. Using $J = 1/2$ and $J' = 3/2$

for the D_2 line, Eq. 4.8 becomes

$$\bar{n}_{2d} = \frac{4}{2/3\,\sigma_0\Gamma} \int df\, D(f). \tag{4.9}$$

Thus, when integrating over the entire D_2 line, Eq. 4.6 is modified by replacing the two-level scattering cross section σ_0 with $2/3\,\sigma_0$.

Calculation of the total flux Consider now a Gaussian light beam with $1/e^2$ radius of r_b, characterized by its intensity

$$I(r) = I_0 \exp\left(-2\frac{r^2}{r_b^2}\right), \tag{4.10}$$

where I_0 is peak intensity and r the distance relative to the center of the beam. The integration over the entire beam yields the total optical power

$$P = I_0 \cdot \pi \left(\frac{r_b}{\sqrt{2}}\right)^2. \tag{4.11}$$

The Gaussian beam can be treated as an effective circular light beam with constant intensity I_0 and a radius of $R = r_b/\sqrt{2}$. Thus, the instantaneous total number of atoms N in the interaction volume of the atomic and the light beam is given by integrating Eq. 4.4 over the effective area of the Gaussian beam:

$$N(x,z) = \bar{n}_{2d}(x,z)\,\pi R^2 \tag{4.12}$$

Here, the time-of-flight of atoms through the interaction volume depends on the displacement relative to the center of the beam. The average time-of-flight is given by $\bar{t}_{tof} = 2\bar{R}/\bar{v}$, where

$$2\bar{R} = \frac{4}{3\pi}\,2R \tag{4.13}$$

is the average distance an atom moves through the light beam[7]. Finally, the flux ϕ through the light beam is given by

$$\phi(x,z) = N(x,z)\,\bar{t}_{tof} = \frac{3\pi^2}{16}\,\bar{n}_{\mathbf{2d}}(x,z)\,2R\,\bar{v}. \tag{4.14}$$

Two cases can be distinguished. The first case, shown schematically in Fig. 4.2b, occurs when the light beam diameter is small compared to the spatial extension of the atomic beam, as it is the case for the Li beam effusing from the exit nozzle. Here, the atomic density can be assumed constant over the light beam area, and Eq. 4.14 can be approximated by the infinitesimal calculation, Eq. 4.5, by replacing $2R$ with dx. By measuring the optical density at different x positions and interpolating between the measurement points, the total flux is obtained by integrating Eq. 4.5 over x:

$$\phi_{tot} = \frac{3\pi^2}{8}\int dx\,\bar{n}_{2d}(x,z)\,\bar{v} \overset{4.9}{=} \frac{9\pi^2\bar{v}}{8\sigma_0\Gamma}\int dx \int df\, D(z,x,f). \tag{4.15}$$

Here, the z dependence cancels out because, while the density is decreasing with increasing z, the atomic beams spatial extension (and thus the integration bounds in

[7] The distance $d(x)$ as a function of the displacement x is given by $d(x) = 2\sqrt{R^2 - x^2}$. The average distance is calculated by $\int_0^R dx\, x\, d(x) / \int_0^R dx\, d(x)$

the x integral) increases, conserving the total number of atoms.

The second case, illustrated in Fig. 4.2c, considers a collimated atomic beam, as it is the case of the Rb beam after the Li reservoir, due to collimation by the intermediate and exit nozzle. If the light beam diameter equals the spatial extension of the atomic beam, the entire atomic beam is probed at once. In this case, the x and z dependence drops out and Eq. 4.14 can be directly used to determine the total flux:

$$\phi_{\text{tot}} \overset{4.9}{=} \frac{9\pi^2 r_{\text{b}} \bar{v}}{4\sqrt{2}\sigma_0 \Gamma} \int df\, D(f). \tag{4.16}$$

4.3 Spectroscopy of the lithium atomic beam

In this section, the results of the characterization of the Li beam during Li-only operation are presented. Transversal absorption spectroscopy is performed in the 6-way cross (Fig. 4.1, path (ii)). Absorption spectra are taken using the measurement scheme shown in Fig 4.2b for different temperatures of the Li reservoir. The $1/e^2$ light beam diameter is $2r_{\text{b}} = 1.04(10)$ mm. The measurement is performed at a distance $z = 71.5(5)$ cm from the end of the exit nozzle. The frequency sweep of the ECDL is done with a repetition rate of 9 Hz over a range of approximately 4 GHz. The time to scan over one natural linewidth of around $2\pi \cdot 6$ MHz (see Tab. 2.2) is therefore approximately 166 µs, while the time of flight of the atoms through the light beam is on the order of $t_{\text{tof}} \sim 650$ ns, based on the theoretically expected average velocities of $\bar{v} \sim 1600$ m/s (Eq. 2.4) in the given temperature range. This means that a single atom of the atomic beam effectively only interacts with a single frequency of the light beam before exiting the interaction volume of the atomic and the light beam. To avoid optical pumping into dark states [24], the optical power has to be chosen low enough that, on average, one photon is scattered per atom. The condition for this is that the product of scattering rate and time of flight is less than or equal than one:

$$1 \overset{!}{=} R_{\text{sc}}\, t_{\text{tof}} \overset{I \ll I_{\text{sat}}}{\approx} \frac{\Gamma}{2} \frac{I}{I_{\text{sat}}} t_{\text{tof}} \simeq 12 \cdot \frac{I}{I_{\text{sat}}} \tag{4.17}$$

This condition corresponds to an optical power of $P \simeq 0.91$ µW[8]. For the calculation, the representative value for I_{sat} from Tab. 2.2 is used. The measurements were performed with 0.80(5) µW.

Fig. 4.3a shows an absorption signal at a temperature of 460 °C in the center of the atomic beam ($x = 0$), together with the reference signal. The absorption signal is an average over 256 traces. The reference signal shown is a polynomial fit to the measured reference signal, adjusted to match the absorption signal at the edges where no absorption occurs. The signals are given in units of the voltage, as measured by the photodiode, which is proportional to the intensity of the light. The linear decrease in intensity with increasing frequency is an artifact of the frequency sweep of the ECDL [33]. The absorption dip is clearly visible, with a width on the order of 1 GHz, such that the hyperfine structure is not resolved. The frequency axis is given relative to the Fabry-Pérot resonance nearest to the absorption dip. Since the finesse of the interferometer is on the order of a few thousand, the uncertainty in the frequency axis is on the order of a few hundred kHz and therefore negligible. Dividing the reference signal by the absorption signal and taking the natural logarithm gives the optical density, shown in Fig. 4.3b.

[8] Using $P = 2I/(\pi r_{\text{b}}^2)$ for a Gaussian beam

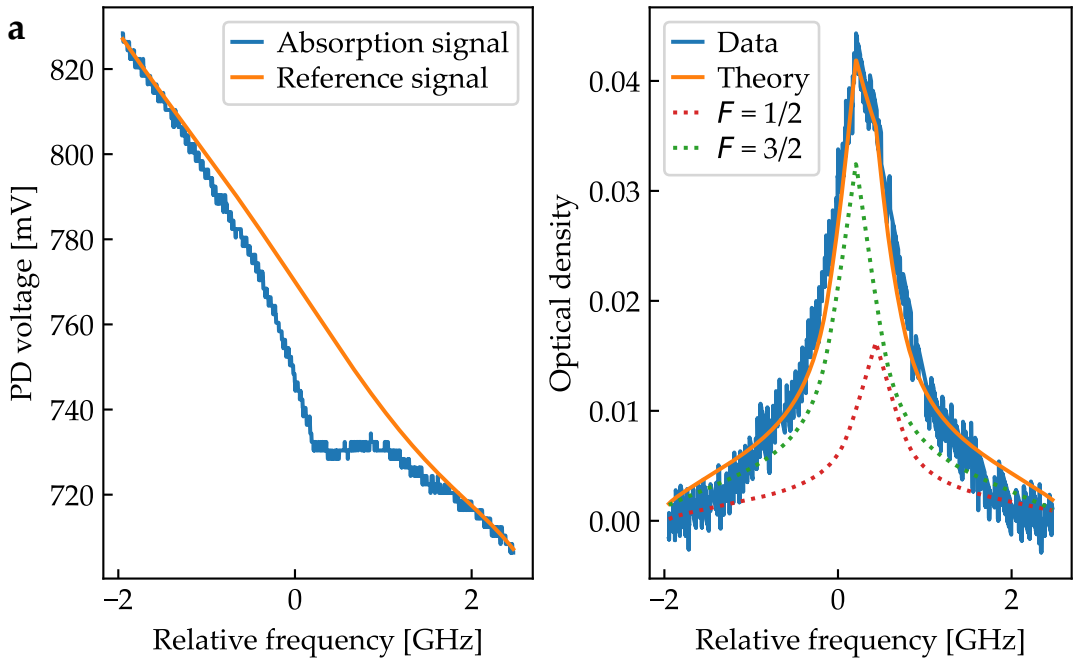

FIGURE 4.3: **a** Measured absorption signal of the D_2 line through the center of the Li atomic beam along path (ii) in Fig. 4.1 at a Li reservoir temperature of 460 °C. The reference signal measures the light intensity without absorption. The linear decrease in intensity for increasing frequency is an artifact of the ECDL. The signal is given in units of voltage as measured by the photodiode (PD), which is proportional to the intensity. **b** The optical density is calculated by taking the natural logarithm of the ratio of the reference signal to the absorption signal. The optical density spectrum is proportional to the angular distribution of atoms due to the Doppler effect. It matches the theoretical expectation, which is the sum of the two contributions from the transitions between the $F = 1/2$ and $F = 3/2$ ground states and the excited state.

Beam divergence The shape of the optical density contains information about the angular distribution of the atomic beam. The measured spectrum is the convolution of the distribution of transverse velocities with the Lorentzian absorption profile, whose width corresponds to the natural linewidth. Since the width of the measured optical density is significantly larger than the natural linewidth, the convolution can be neglected and the absorption cross section can be assumed as an effective δ-distribution. Within this approximation, the measured spectrum is equivalent to the transverse velocity distribution.

Assuming molecular flow, an atom effusing from the orifice with average velocity $\bar{v}$ at an angle θ is moving along a straight line with constant transverse velocity $v_{\parallel} = \bar{v}\sin(\theta)$. According to the Doppler effect, Eq. 2.25, this corresponds to a resonance frequency of $\omega = \omega_0 + k\bar{v}\sin(\theta)$ or equivalently, using $\omega = 2\pi f$ and $k = 2\pi/\lambda_0$,

$$f = f_0 + \frac{\bar{v}\sin(\theta)}{\lambda_0}. \tag{4.18}$$

The theoretically expected distribution is known from section 2.1 and it has a $1/e^2$ divergence angle of $2 \cdot 574\,\text{mrad}$. It can be converted into an expected frequency spectrum using Eq. 4.18, as shown in Fig. 4.3b. The exit nozzle is approximated as

point-like due to the large distance between the interaction volume and the nozzle diameter. The spectrum is the sum of the two transitions $F = 1/2 \rightarrow F' = 1/2, 3/2$ and $F = 3/2 \rightarrow F' = 3/2, 5/2$, where the excited states are treated as one effective state due to the small frequency splitting (see Fig. 2.3). Since the thermal energy of the atoms ($k_B \cdot 460\,°\mathrm{C} \simeq h \cdot 15\,\mathrm{THz}$) is much larger than the hyperfine splitting of the ground state, all atoms are equally distributed among the substates. The relative ratio of the two transitions is therefore simply given by the ratio of the number of m_F substates. which is two in this case. The absolute amplitude is adjusted such that the sum of both contributions is normalized to the measured optical density. There is good agreement between theory and experiment, indicating that the angular distribution of atoms matches the theory. It appears that the actual divergence is slightly larger than predicted by the theory, which is due to the small effect of a non point-like orifice. There are small deviations at larger angles, which are caused by the clipping of the atomic beam at the walls of the 6-way cross. Note that the agreement is quit good, despite the mean free path at this temperature being approximately 10 mm, indicating that the system is already partially in the continuum flow regime.

Total flux The total flux of atoms effusing from the Li reservoir can be estimated using Eq. 4.15. To do this, the optical density integrated over the frequency is measured as a function of the distance x from the center of the atomic beam. The results for a temperature of 460 °C are shown in Fig. 4.4a. The integration is performed numerically on the optical density spectrum, where the noise was previously filtered out using a rolling average. The uncertainty mainly arises from the procedure of adjusting the reference signal to the absorption signal. To account for these uncertainties, a statistical average over eight data sets is utilized. The uncertainty in the x-direction is ± 0.5 mm, which is due to the alignment of the light beam.

The figure shows the expected decrease in flux with increasing distance, consistent with the angular distribution of the atomic beam. This behavior is independent of temperature as long as the as the source operates in the molecular flow regime. The x-integral in Eq. 4.15 is done using a heuristic quadratic fit to the data. The integral can be written as

$$\int dx\, D(x) = D(0) \cdot \Delta x, \tag{4.19}$$

where $D(0)$ is the optical density measured at the center of the atomic beam, and Δx is a factor determined by the fit. For this data set, $\Delta x = 29.7(14)$ mm, which is consistent with values measured for other temperatures.

To compare theory and experiment it must be considered that the part of the atomic beam with an angle larger than $\theta_0 = 17.8\,°$ hits the vacuum tube of the 6-way cross. The fraction of atoms with $\theta_0 < 17.8\,°$ is calculated by integrating the theoretical angular distribution $j(\theta)$ over the solid angle up to θ_0 and normalizing it by the integral over the entire solid angle:

$$\frac{2\pi \int_0^{\theta_0} d\theta\, \sin(\theta)\, j(\theta)}{2\pi \int_0^{\pi/2} d\theta\, \sin(\theta)\, j(\theta)} \simeq 0.23. \tag{4.20}$$

It is assumed that atoms hitting the walls stick to them and do not contribute to the measured optical density. This assumption is justified by the fact that the 6-way cross is at lower temperature compared to the Li reservoir, and therefore the vapor pressure of these atoms is negligible. The total measured flux, corrected by

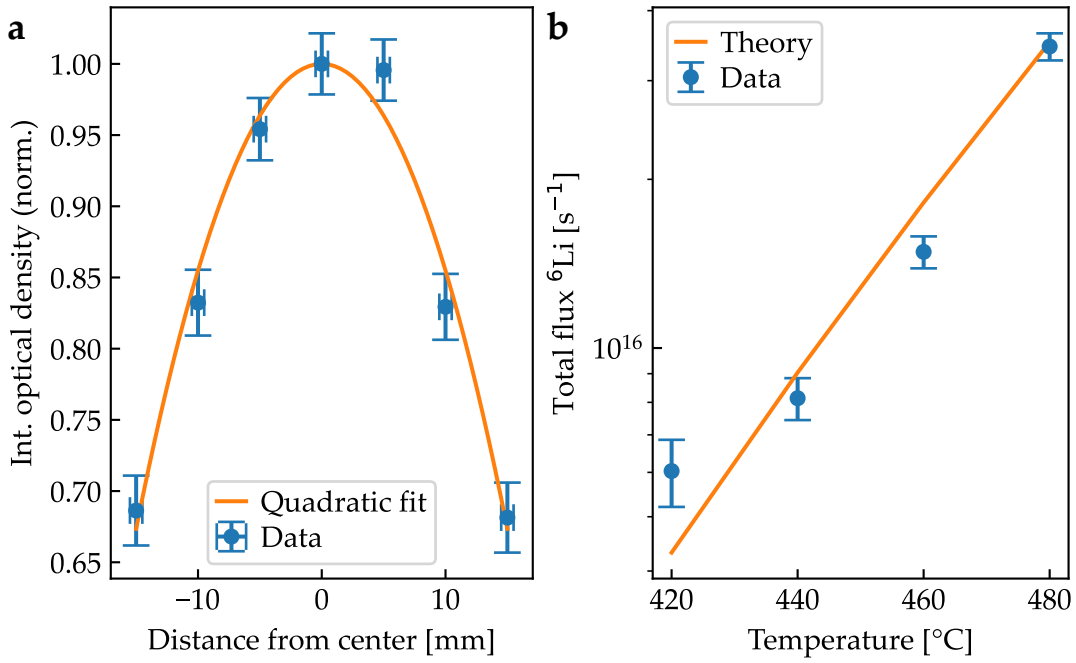

FIGURE 4.4: **a** Integrated optical density $\int df\, D(f)$ at a temperature of 460 °C as a function of the distance from the center of the atomic beam, normalized to its value at the center. A heuristic quadratic fit is utilized, needed for the calculation of the **b** Total flux in dependence of the temperature. The experimental flux is determined using Eq. 4.15, the theoretical curve is calculated with Eq. 2.11.

this factor, is shown in Fig. 4.4b. It was calculated using the theoretical average velocity. The data points represent a statistical average over eight data sets. The uncertainty is given by the standard deviation combined with the uncertainty in Δx. The theoretical flux is calculated using Eq. 2.11.

The experimentally determined flux agrees with the theoretical expectation. The value for a temperature of 450 °C is slightly larger due to a small signal at this temperature, which leads to an overfitting of the data.

Expected MOT loading rate The key quantity in an ultracold atom experiment is the MOT loading rate. In the following, the expected MOT loading rate is estimated, taking into account the geometry of the vacuum system of the planned main experiment [17]. Due to this geometry, only the part of the atomic beam with an angle smaller than $\theta_{\mathrm{MOT}} = 6$ mrad can, in principle, reach the MOT. All other atoms stick to the walls. Calculating analogously to Eq. 4.20 the fraction of atoms gives $2.25 \cdot 10^{-4}$. The expected flux into the MOT plane is then given by the total flux multiplied by this factor. For a temperature of 400 °C, this gives a value of $4.4 \cdot 10^{11}\,\mathrm{s}^{-1}$. When additional losses in the Zeeman slower are considered, this results in an expected MOT loading rate of $2.7 \cdot 10^{9}\,\mathrm{s}^{-1}$. The losses in the Zeeman slower are due to the maximum capture velocity (a factor of 0.03) and transverse heating during the cooling process (a factor of 0.2) [17]. A similar calculation for 450 °C results in an expected MOT loading rate of $1.7 \cdot 10^{10}\,\mathrm{s}^{-1}$.

A practical importance also lies in the expected lifetime of the reservoir. This can be estimated by dividing the total effused flux by the total number of atoms in the reservoir. A chunk with a mass of 10 g and 95 % ^{6}Li contains approximately $9.5 \cdot 10^{23}$ ^{6}Li atoms. At 400 °C, the total flux effusing from the exit nozzle is $2{,}0 \cdot 10^{15} s^{-1}$

and from the intermediate nozzle $0{,}7 \cdot 10^{15} s^{-1}$. This gives an expected lifetime of 101 000 hours. At 450 °C, the lifetime is expected to be 15 000 hours.

4.4 Spectroscopy of the rubidium atomic beam

In this section, the results of the characterization of the Rb beam during Rb-only operation are presented. Transversal absorption spectroscopy is done in the 6-way cross (Fig. 4.1, path (ii)) and in the middle section (Fig. 4.1, path (i)). In the end, the total flux of ^{87}Rb after the Li reservoir is of interest. As a preview, the Rb beam in the original design did not perform as expected (subsection 4.4.1), which led to modifications in the original source design, discussed in subsection 4.4.2.

4.4.1 Original source design

Total flux after the Li reservoir The atomic beam is collimated after the Li reservoir due to the intermediate and exit nozzle. The maximum angle an atom can have to pass the nozzles is 7.6 mrad. Assuming a $\cos(\theta)$ angular distribution of the small Rb nozzle[9], the fraction of atoms relative to the total flux which pass through the nozzles is $5.82 \cdot 10^{-5}$ using Eq. 4.20. At the distance 71.5(5) mm after the exit nozzle the atomic beam has an expected beam diameter of 6.0 mm. Therefore, the measurement scheme shown in Fig. 4.2c is applied, and Eq. 4.16 can be used to calculate the total flux.

A 1.25(7) mm beam is expanded to a $1/e^2$ beam diameter of $2r_\mathrm{b} = 6.05(5)$ mm using the telescope shown in Fig. 4.1. Analogous to the Li beam measurement, the measurement parameters are set such that an atom propagating through the light beam interacts effectively with only a single frequency during the time of flight and scatters on average one photon. A ^{87}Rb atom at 100 °C has a theoretical average velocity of 301 m/s, resulting in a time of flight of approximately 20 µs. The frequency is scanned over roughly 300 MHz with a repetition rate of 9 Hz, resulting in a time of 2 ms to scan over one natural linewidth, which is much longer than the time of flight. Condition Eq. 4.17 limits the optical power to less than 0.96 µW. For this measurement, an optical power of 0.90(5) µW is used.

The optical density is determined from the absorption signal in the same way as for Li, except that this time the reference signal is determined not by measurement but by directly fitting a polynomial to the regions of the absorption signal without absorption. The measured optical density, averaged over 256 traces, for the transition from the ground state $F = 3$ to the excited states $F' = 2, 3, 4$ of ^{85}Rb is shown in Fig. 4.5a at a temperature of 225 °C. The optical density is low due to the small number of Rb atoms passing through the nozzles. Each hyperfine transition is resolved in the spectrum, and the relative heights correspond to the transition strengths $S_{FF'}$. The width of the transitions is on the order of the natural linewidth, with no additional Doppler broadening, confirming the collimation of the atomic beam. This is additionally confirmed by displacing the light beam off center, which leads to the disappearance of the signal.

The total flux of ^{87}Rb is calculated by integrating the optical density over the entire D_2 line. However, due to the weak signal, it is impractical to do this directly. To improve the signal-to-noise ratio, the frequency sweep is not done over the entire D_2 line, but is instead restricted to the $F = 3 \rightarrow F' = 2,\ 3,\ 4$ transitions of ^{85}Rb.

[9] The $\cos(\theta)$ angular distribution is assumed because the formulas for the modified angular distribution are only valid for long tubes

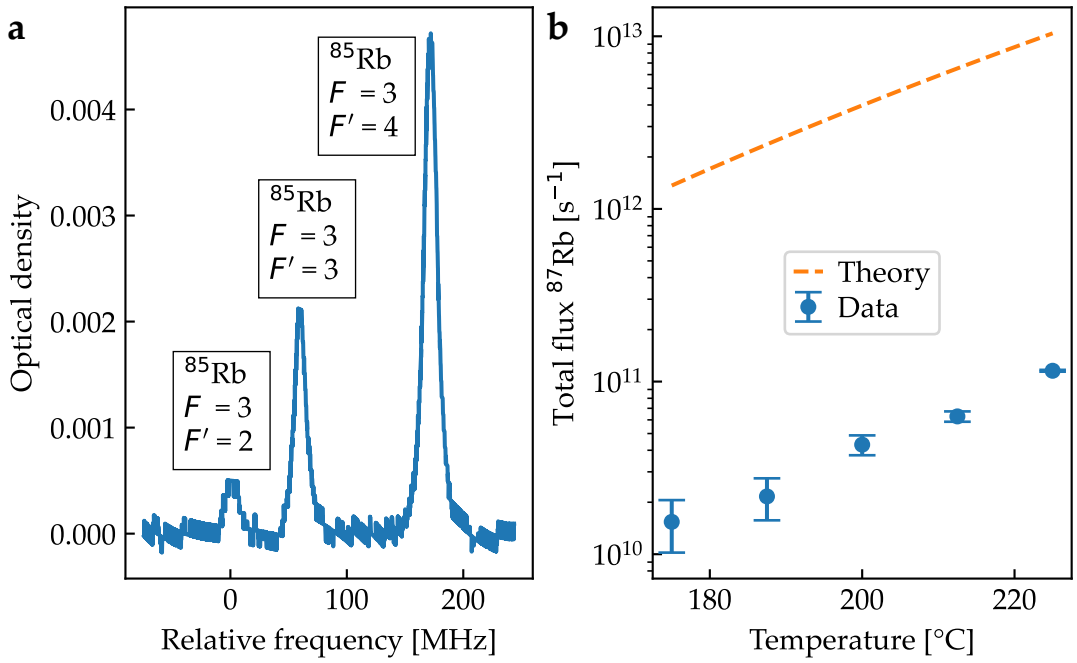

FIGURE 4.5: **a** Optical density spectrum of the $F = 3 \rightarrow F' = 2, 3, 4$ transition of the D_2 line in ^{85}Rb after the Li reservoir at a temperature of 225 °C. Since the Rb beam is collimated, no further Doppler broadening occurs, so the width of the peaks is on the order of the natural linewidth. The relative heights are determined by the transition strengths $S_{FF'}$. **b** Total flux of ^{87}Rb after the Li reservoir as a function of the Rb reservoir temperature, calculated from the optical density spectrum and Eq. 4.16. The large discrepancy of two orders of magnitude compared to the theoretical expectation is discussed in the text.

This approach reduces noise due to the smaller sweep range and takes advantage of the higher natural abundance of ^{85}Rb compared to ^{87}Rb. By integrating over the $F = 3 \rightarrow F' = 2, 3, 4$ transitions, the total flux of ^{85}Rb atoms in the ground state $F = 3$ is obtained. The integration is performed by fitting a Gaussian function to the data. Since the thermal energy of the atoms is much larger than the hyperfine splitting of the ground state, all atoms are equally distributed among the substates. The ratio of the density of atoms in the ground states $F = 3$ and $F = 2$ is therefore given by the ratio of the number of m_F states. The $F = 3$ level has seven substates and the $F = 2$ has five. Thus, the total flux of ^{85}Rb atoms is 12/7 times the flux of ^{85}Rb atoms in the ground state $F = 3$. The total flux of ^{87}Rb atoms is then determined based on the relative natural abundance.

The total flux of ^{87}Rb is calculated in this way and shown in Fig. 4.5 for different Rb reservoir temperatures. The temperature of 175 °C is the lowest temperature where a signal could be detected. The uncertainty is given by the standard deviation from the statistical average over eight data sets. The theoretical expectation is calculated using Eq. 2.10 together with the factor of $5.82 \cdot 10^{-5}$ of atoms that theoretically pass the exit nozzle. More specifically, since the formulas are only valid in the molecular flow regime, which is valid up to 118 °C, the theoretical prediction is an extrapolation of the molecular flow regime.

There is a significant discrepancy of two orders of magnitude between the measurement and theory. Although it is expected that the atomic beam has a higher

divergence in the continuum flow regime due to collisions, which would result in fewer atoms making it through the exit nozzle, this cannot fully explain the difference here. Specifically, if the source was operating correctly in the molecular flow regime, the theoretical flux at 100 °C should be approximately $5 \cdot 10^{11}\,\mathrm{s}^{-1}$, a value high enough to be measurable. However, there is no signal at 100 °C, indicating that the flux at this temperature must be at least an order of magnitude smaller. To better understand what is happening, the beam must be measured in the middle section.

Total flux in front of the Li reservoir A light beam with 1.25(7) mm diameter is used, and the optical power is set to 0.17(1) µW to avoid optical pumping. The same measurements as for the Li beam were performed, i.e. the absorption spectrum was measured for different distances from the center of the atomic beam to calculate the total flux. Additionally, the spectra should contain the information about the angular distribution. However, specific challenges arise in the case of Rb, which will be discussed below.

During the operation of the Rb or Li reservoir, source material accumulates inside the vacuum system. For a fixed temperature, an equilibrium is reached between the number of atoms effusing from the reservoir and the number of atoms being pumped into the ion pump, leading to a certain vapor pressure of Rb or Li background gas. Therefore, an absorption signal is the sum of contributions from both the atomic beam and this background gas. In the case of Li, this does not seem to be a problem due to its relatively low vapor pressure. Under the assumption that Li atoms thermalize with the walls of the 6-way cross at lower temperatures, background Li has such a low vapor pressure that it does not contribute measurably to the absorption signal. However, for Rb, problems begin to arise because its vapor pressure at room temperature is already high enough to noticeably affect the absorption spectrum. While this is not an issue for Rb in the 6-way cross due to the small flux of atoms into it, in the middle section, a significant accumulation of atoms occur. Therefore, special care must be taken when interpreting the spectra.

The spectrum of the optical density over the full D_2 line of both isotopes at a temperature of 100 °C is shown in Fig. 4.6. The spectrum consists of four peaks corresponding to transitions from both ground states to the excited states for each isotope. Unlike for the Rb beam after the Li reservoir, the hyperfine splitting of the excited states is not resolved due to Doppler broadening. A fit function is applied to the data, where each peak consist of the sum of three Gaussian functions, leading to a total sum of 12 Gaussian function, all with the same full width at half maximum. A full width at half maximum of 578(23) MHz is obtained from the data, independent of the temperature in the range from 50 °C to 225 °C. The theoretical full width at half maximum for a $\cos(\theta)$ angular distribution is 630 MHz at 50 °C and increases with temperature due to the increasing average velocity. The middle section is approximately at room temperature, where the theoretical Doppler width for room-temperature Rb vapor is 509 MHz [24]. The measured width lies between the theoretical expectations of the angular distribution of the atomic beam and the Doppler width, indicating that the spectrum likely represents a mixture of both.

To calculate the total flux, Eq. 4.15 is used, where the optical density should ideally be measured at different distances from the center of the atomic beam, as done for Li in Fig. 4.4a. However, for Rb, the outcome of this measurement is correlated with the temporal order in which the measurements are taken due to the accumulation of Rb. For the calculation, it is thus assumed that the optical density remains constant as a function of the distance, with $\Delta x = 34.4\,\mathrm{mm}$ (see Eq. 4.19)

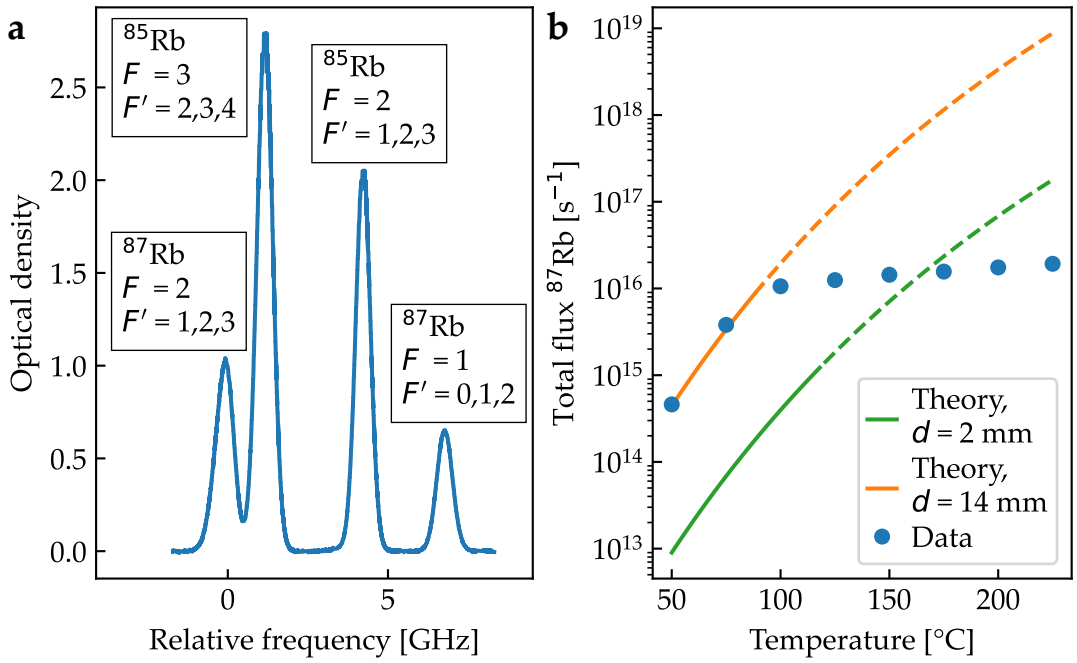

FIGURE 4.6: **a** Spectrum of the optical density of the entire D_2 line of ^{85}Rb and ^{87}Rb at a Rb reservoir temperature of 100 °C in front of the Li reservoir. The hyperfine splitting of the ground states for each isotope is resolved, while the hyperfine splitting of the excited states is not resolved due to Doppler broadening. **b** Total flux effusing from the Rb reservoir, calculated using Eq. 4.15 as a function of the Rb reservoir temperature. No error bars are shown due to large systematic uncertainties, as described in the text. The data points provide only a rough estimate. The theory is calculated using Eq. 2.10, assuming two different orifice diameters d. The transition from the solid line into the dashed line marks the transition from the molecular to the continuum flow regime.

approximated as the entire width of the vacuum tube. To minimize the contribution to the optical density from the background vapor, the following measurement procedure is performed: First, when the source is at room temperature, it is verified that the background density is small and no absorption is observed. Then, the Rb reservoir is heated to the desired temperature, and the optical density is measured immediately after reaching this temperature. The measured optical density is then converted to a flux using Eq. 4.15, assuming that the optical density arises from a directed flux of atoms. This estimation is rather rough, and precise values should not be expected, but it provides a general guide to the behavior of the system.

The total flux measured in this way is shown in Fig. 4.6b. The data points are presented without error bars due to the large systematic uncertainties in the calculation, however, they offer an order-of-magnitude estimate. The theoretical total flux is calculated with Eq. 2.10, assuming two different scenarios: one where the total flux is determined by the small orifice with a diameter of $d = 2\,\text{mm}$ and another where the flux is given by the large opening of the cylinder with a diameter of $d = 14\,\text{mm}$.

Two unexpected phenomena are observed: First, at lower temperatures, the flux seems to follow the theoretical expectation based on the larger cylinder rather than the smaller orifice[10]. This is surprising because, although it is possible for the orifice

[10]The fact that they coincide is likely accidental due to the large uncertainties

to load atoms with a large angle θ into the cylinder, the total output rate from the cylinder should not exceed the input rate from the orifice. This suggests that these Rb atoms may have another origin. It is likely that Rb atoms in the cylinder are being loaded from background Rb remaining from previous measurement cycles.

The second unexpected observation is a noticeable flattening in the total flux at around 90 °C, after which the total flux increases very slowly. Interestingly, the flattening occurs roughly at a temperature where the mean free path of the atoms become equal to the diameter of the cylinder, which is expected at 88 °C. This suggests that the total flux is dominated by the big cylinder, which acts as kind of a source itself. The flattening in the flux could indicate the onset of the continuum flow regime, where atoms effusing directly from the orifice begin to collide with other Rb atoms in the cylinder, therefore reducing the flux in the collimated atomic beam.

Although this interpretation is quit imprecise due to the systematic errors, it offers a rough idea that the cylinder is causing the issue of low flux. It is likely not a problem with the cylinder alone, but rather a combined issue involving both the cylinder and the background vapor. In the current main experiment, where this nozzle is used, no such effect was observed. The key difference in the main experiment is the inclusion of an additional cold nozzle, operated at approximately -5 °C and located after the Rb reservoir [17]. Originally intended to protect the ion pump from long-term Rb exposure, this cold nozzle also reduces the background Rb pressure. However, in a first step, only the nozzle design was modified. The subsequent changes to the source are described in the next section.

4.4.2 Updated source design

In the previous section, it was shown that the flux of Rb atoms through the exit nozzle is much lower than expected. The issue was believed to originate from the cylinder surrounding the Rb orifice. The obvious solution is to get rid of it, and thus, the design of the Rb nozzle was changed. The updated version is shown in Fig. 4.7 in comparison with the old design. Most of the setup remained unchanged, but slight modifications were made to the Rb reservoir and the middle section. The new orifice has the same dimensions as the old one (2 mm diameter and 1 mm width), but this time without the cylinder. Instead of welding the new nozzle into the 4-way cross, the orifice is drilled into a double-faced flange[11] and placed between the two 4-way crosses of the Rb reservoir and the middle section. The cone-like structure inside is designed for better heat conductivity, but has no influence on the atomic beam since it is located within the reservoir. Additionally, the bellow is removed, because it was found during operation that alignment is not critical and the fabrication precision exceeds the required precision. This allowed the Rb reservoir to be positioned closer to the Li reservoir, resulting in a higher fraction of atoms passing through the nozzles. The maximum divergence angle increases from $2 \cdot 7.6$ mrad to $2 \cdot 10.3$ mrad, resulting in fraction of $1.07 \cdot 10^{-4}$ atoms ideally passing through the nozzles, which is almost twice as much as in the old design.

With the new Rb nozzle design, the total flux is measured again. The measurement is performed exactly as before, without further modifications. The results for the total flux in front of and after the Li reservoir are shown in Fig. 4.8.

[11] Kurt J. Lesker: DFF275X000

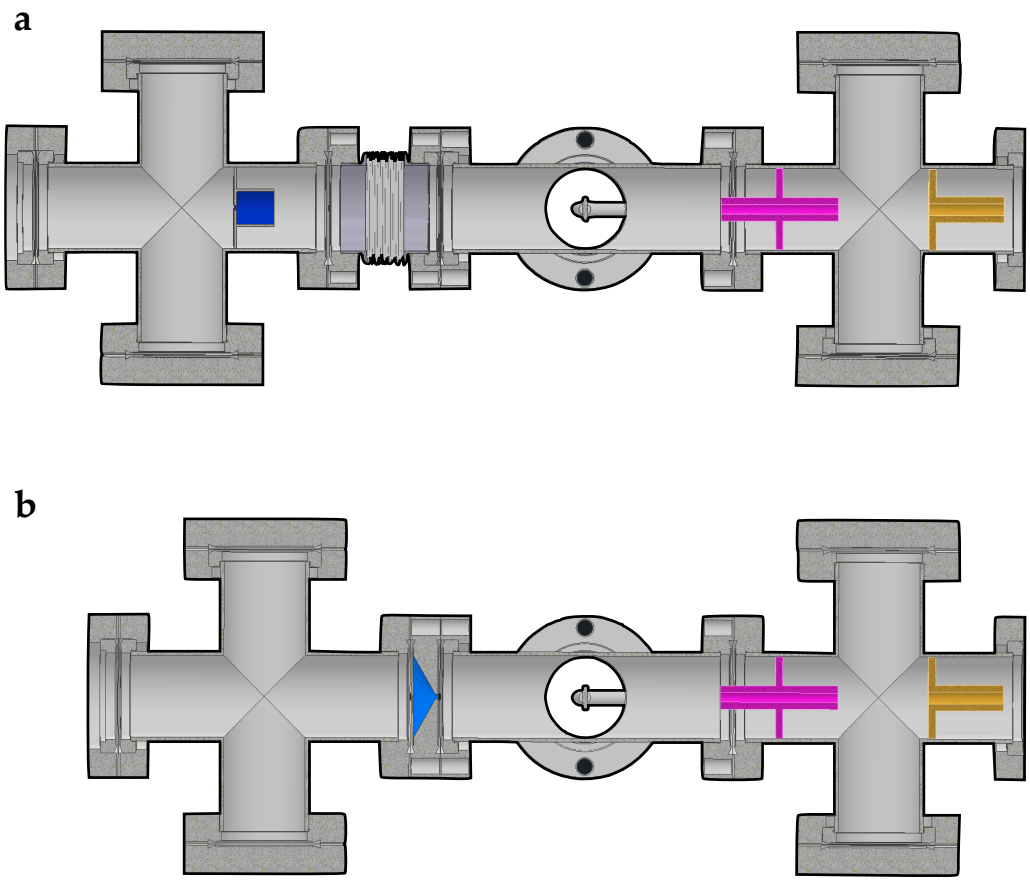

FIGURE 4.7: **a** Original design of the source and **b** updated design after performing spectroscopy of the Rb beam. The nozzle in the Rb reservoir, consisting of a small orifice and a surrounding cylinder, is replaced with a nozzle that lacks the cylinder. Instead of welding the nozzle into the 4-way cross of the Rb reservoir, the new nozzle is drilled into a double-faced flange connected to the reservoir. The nozzle has a cone-like structure from the inside for better heat conductivity. Additionally, the bellow was removed, allowing the nozzle to be positioned closer to the Li reservoir, resulting in a higher fraction of atoms passing through the exit nozzle.

Total flux The flux in front of the Li reservoir follows now the theoretical expectation of the small orifice. Notably, the flattening of the flux for temperatures above 100 °C no longer occurs, and for temperatures above 150 °C, the flux even reaches higher values than before. The flux after the exit nozzle increased significantly compared to the old design, though there is still some deviation between the measurement and theory. At a temperature of 100 °C, the measured flux is lower than the theoretical prediction by a factor of three. The discrepancy increases with higher temperatures, likely due to the source entering the continuum flow regime at temperatures above 118 °C.

Three possible explanations could account for the discrepancy. First, the theoretical flux was calculated using Eq. 2.10, which assumes an infinitely-thin orifice. A more precise estimation would include the Clausing factor (Eq. 2.12), though this equation applies only to orifices with large aspect ratios. Using the equation nonetheless results in a Clausing factor of 3/8, which should be seen as a lower bound for the real value. Another likely reason for the smaller flux could be collisions with the background Rb atoms. Finally, it is possible that the angular distribution of atoms effusing from the reservoir differs from the theoretical expectation, although this cannot be experimentally confirmed.

Expected MOT loading rate For a temperature of 100 °C, the experimentally determined total flux after the Li reservoir is approximately $1{,}4 \cdot 10^{10}\, s^{-1}$, and the total divergence angle is $2 \cdot 10.3$ mrad. The geometry of the vacuum system of the planned main experiment restricts atoms with an angle larger than 5 mrad from reaching the MOT, reducing the MOT loading rate by a factor of four compared to the given value of the flux. Taking into account additional losses in the Zeeman slower (a factor of 0.3 due to the maximum capture velocity and a factor of 0.4 due to the transverse heating), the expected experimental MOT loading rate is approximately $4.2 \cdot 10^8\, s^{-1}$, while the theoretical MOT loading rate would be $1.2 \cdot 10^9\, s^{-1}$. For a temperature of 120 °C, an expected MOT loading rate of $9.6 \cdot 10^8\, s^{-1}$ is predicted, approximately a factor of four smaller than the theoretical value. The expected lifetime of the source, using 10 g of Rb in its natural abundance, is estimated to be 13 500 hours at 100 °C and 3900 hours at 120 °C. The MOT loading rate could be further increased using higher Rb reservoir temperatures, but this would reduce the source's lifetime too much.

4.5 Dual-species operation

Since the fluxes and divergences of both atomic beams in single-species operation have been confirmed, up to a small deviation in the flux of Rb, the characteristics of the beams during dual-species operation can now be investigated. In the following, the flux of both Li and Rb as a function of both reservoir temperatures are discussed. At this stage of the experiment, the source had been running for some time. A steady-state pressure of approximately $5 \cdot 10^{-7}$ mbar formed in the middle section, even without the Rb reservoir being actively operated. This pressure corresponds to the vapor pressure of Rb at room temperature, suggesting that the ion pump's performance had degraded. As a consequence, a high Rb vapor pressure remained in the middle section. Although an increased pressure was also observed in the 6-way cross, the Li reservoir's two nozzles, acting as differential pumping tubes, reduced the pressure measured here to approximately $1 \cdot 10^{-8}$, mbar. This will be of importance in the following considerations.

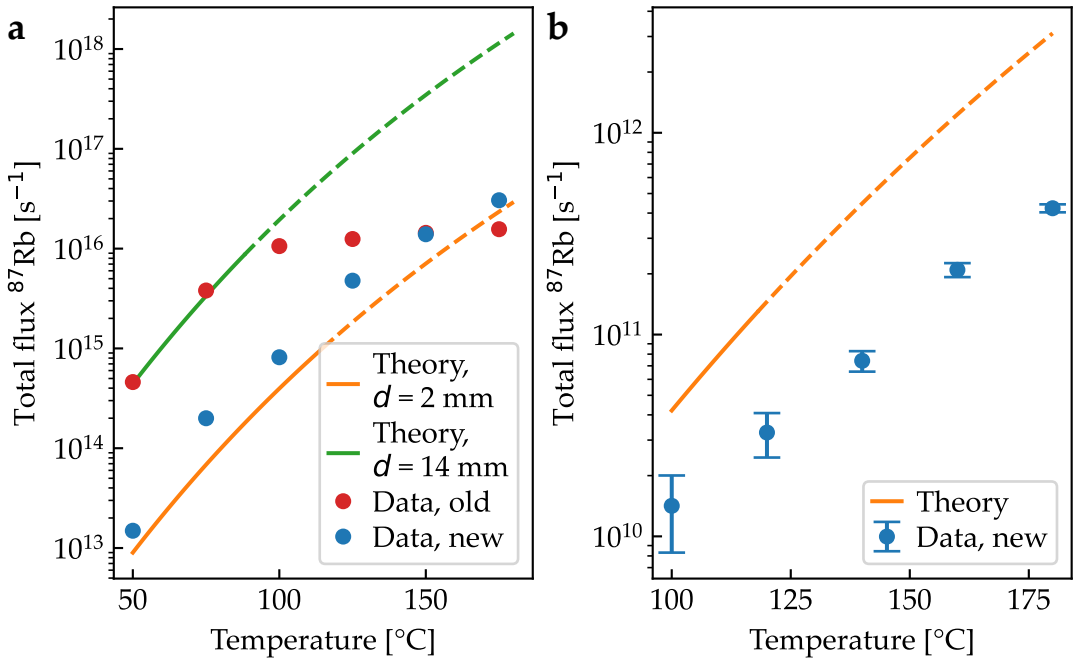

FIGURE 4.8: Total flux of ^{87}Rb as a function of temperature **a** in front of and **b** after the Li reservoir, comparing the performance of the old and the new Rb nozzle designs.

Total flux of the Rb beam in dependence of the Li reservoir temperature The Rb flux after the Li reservoir is measured for three different Rb reservoir temperatures of 140 °C, 160 °C and 180 °C as a function of the Li reservoir temperature, varying from room temperature up to 450 °C. The measurement setup and flux calculation is performed in the same way as in previous sections.

Before discussing the total flux, it is also insightful to examine the absorption spectra at different temperatures of the Li reservoir, for example at 25 °C (Fig. 4.9a) and after heating to 150 °C (Fig. 4.9b). The Rb reservoir is at a temperature of 180 °C. The absorption signal at 25 °C shows the absorption dips of the transitions on top of an almost linear baseline, as expected from the frequency sweep of the ECDL. The baseline has a slight Gaussian form due to a weak background vapor pressure of Rb in the 6-way cross. In contrast, at 150 °C, the absorption signal is dominated by a large Gaussian background caused by the Rb vapor being pumped through the hot Li reservoir, while the beam's contribution remains constant. Due to the heat flow from the Li reservoir, the middle section is also heated during the operation. Since more Rb is accumulated in the middle section compared to the 6-way cross, the pressure gradient between the two increases, and thereby Rb atoms are pumped through the hot Li reservoir.

The flux of ^{87}Rb atoms as a function of the Li reservoir temperature T_{Li} is presented in Fig. 4.10a for three different Rb reservoir temperatures. For temperatures below approximately 300 °C, the flux is constant and is consistent with the values observed during single-species operation. The fluctuations seen are due to a higher uncertainty in the procedure of fitting the baseline, resulting from the strong Gaussian background. Since the flux remains constant, it can be concluded that the background Rb pumped through the Li reservoir does not affect the collimated beam.

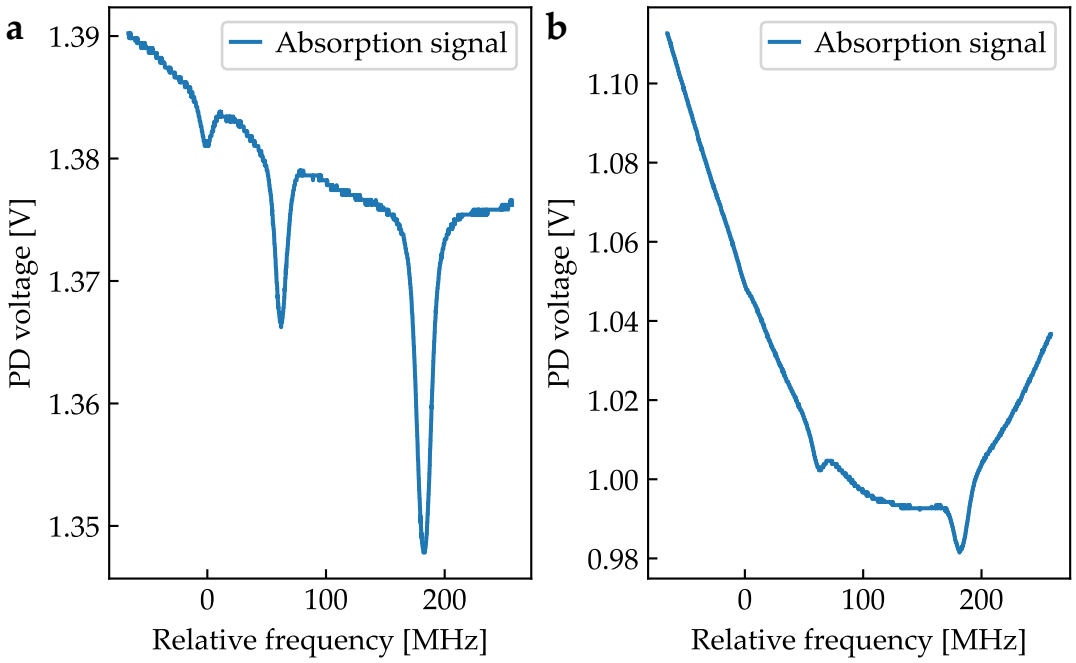

FIGURE 4.9: Absorption signals of the ^{85}Rb $F = 3 \rightarrow 2,\ 3,\ 4$ transition at a Rb reservoir of 180 °C and a Li reservoir temperatures of **a** 25 °C and **b** 150 °C. The effect of Rb background pumped through the hot Li reservoir is indicated by the large Gaussian background signal, while the contribution from the atomic beam itself remains constant.

Above 300 °C, the flux starts to decrease because of the increasing number of collisions with Li atoms, while the beam divergence is not affected. The decrease is the same for all Rb reservoir temperatures. To compare the measurements with theory, the total flux for all Rb reservoir temperatures is normalized to the values for $T_{\mathrm{Li}} < 300\,°\mathrm{C}$ and plotted in Fig. 4.10b, together with the theoretical expectation.

Theoretical predictions are made using a simple model. Consider a beam of Rb atoms with flux ϕ_{in} and average velocity $\bar{v}_{\mathrm{Rb}}$, traveling a distance x through a gas of Li with density n_{Li} and average velocity $\bar{v}_{\mathrm{Li}}$. The reduction in flux to a value of ϕ_{out} due to collisions is given by [21]

$$\frac{\phi_{\mathrm{out}}}{\phi_{\mathrm{in}}} = \exp\left(-\sqrt{2}\sigma n_{\mathrm{Li}} x\right), \tag{4.21}$$

where σ is the scattering cross section introduced in Eq. 2.5. The average relative velocity is approximately given by [36]

$$\bar{v}_{\mathrm{rel}} = \bar{v}_{\mathrm{Li}} + \frac{\bar{v}_{\mathrm{Rb}}^2}{3\bar{v}_{\mathrm{Li}}}, \tag{4.22}$$

with an accuracy of ±5 %. The C_6 coefficient for Rb-Li scattering is taken from Tab. 2.3 and $x = 38.8\,\mathrm{mm}$ is the distance between the intermediate and the exit nozzle.

There is good agreement between theory and experiment. Collisions within the nozzles are not accounted for, though the data suggest they are negligible, likely because the nozzles operate in the molecular flow regime. Attempting to fit Eq. 4.21 to the data, with the C_6 coefficient as a free parameter to extract its experimental value proves unfeasible. The temperature at which the flux drops by half depends mostly on the density of Li atoms than on the C_6 coefficient, because the scattering

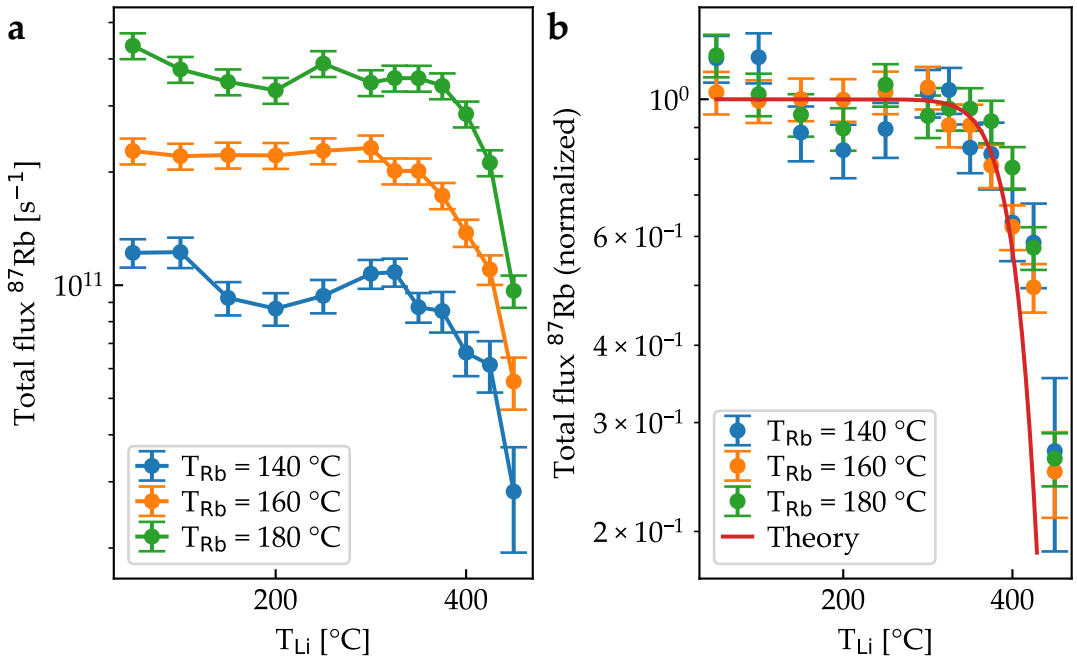

FIGURE 4.10: **a** Total flux of the collimated Rb beam as a function of the Li reservoir temperature T_{Li} for different Rb reservoir temperatures T_{Rb}. **b** Total flux normalized to the mean of the corresponding values for $T_{Li} < 300\,°C$. The flux decreases due to collisions with the Li atoms, and this decrease is independent of the Rb reservoir temperature. A simple theoretical model of the system, described by Eq. 4.21, aligns well with the data. A drop by half is observed at a Li reservoir temperature of around 400 °C.

cross section scales with $C_6^{2/5}$, while the density scales exponential. Consequently, two different C_6 coefficients, differing by an order of magnitude, still align with data within the measurement precision.

Total flux of the Li beam in dependence of the Rb reservoir temperature The Li flux is measured for three different Li reservoir temperatures of 440 °C, 460 °C and 480 °C as a function of the Rb reservoir temperature, which ranged from 100 °C to 180 °C. Measurements at lower Rb reservoir temperatures were avoided to prevent clogging of the Rb nozzle. The measurement setup and flux calculation is performed in the same way as described in previous sections. The expectation is that the collimated Rb beam would not affect the Li flux, given the relatively low flux of Rb.

However, it was observed that the Li flux is influenced in a non-trivial way, depending on the temporal order in which the temperature series is performed and the pre-history of the source. In different measurements with identical parameters, varying trends were observed: sometimes the flux decreased with increasing temperature, sometimes it increased, and sometimes it remained constant. Since this behavior is not physically intuitive, it is clear that a dependence on time and the past state of the system must be present. To illustrate this, Fig. 4.11 shows a time-dependent measurement under specifically chosen conditions. The figure displays the total flux of Li as a function of time and Rb reservoir temperature at a fixed Li reservoir temperature of 460 °C. The day before, the Li reservoir had been operated at high temperature. Initially, the Li reservoir is heated to the desired temperature,

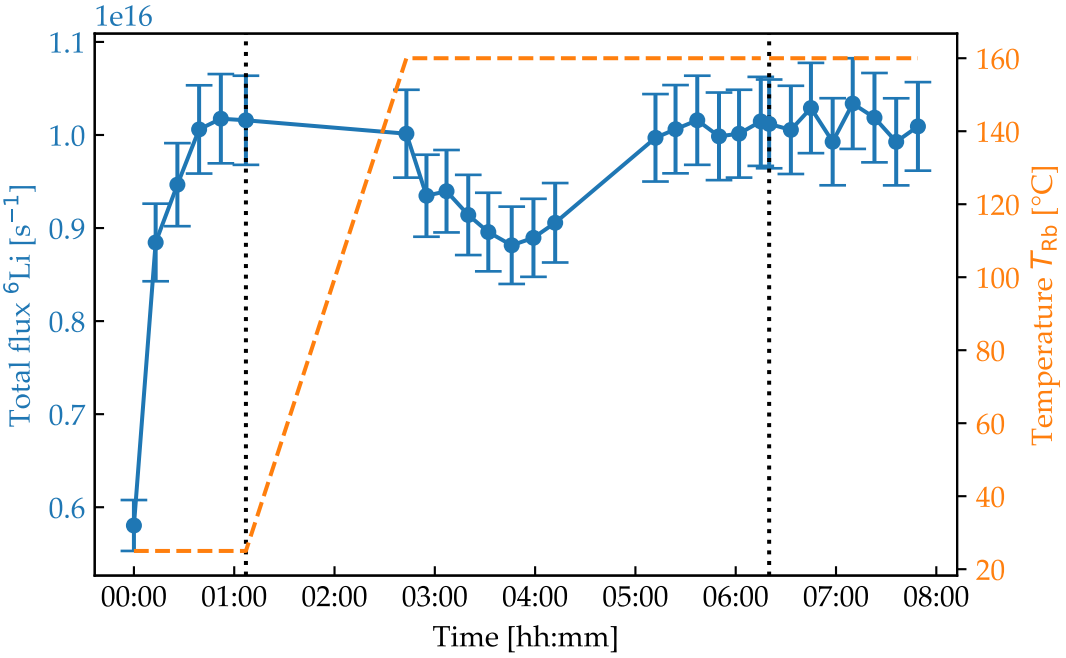

FIGURE 4.11: Time-dependent measurement of the Li flux at a fixed Li reservoir temperature of 460 °C and two different temperatures of the Rb reservoir (room temperature and 160 °). The figure is divided into three regions, marked by the black dotted lines. In the first region, the thermalization of the Li reservoir over approximately 50 min is shown. Next, the Rb section is heated, resulting in a dip in the Li flux with an amplitude of around 10 % over a time scale of 2 hours, before returning to its original value. Up to this point, the shutter in the middle section remained closed, such that this effect can be attributed to the Rb background. In the third region, the shutter is opened, allowing the collimated Rb beam to pass through the Li reservoir, but the Li flux remains unchanged.

while the Rb reservoir remains at room temperature. The shutter in the middle section is closed. The time zero is set to the moment when the Li reservoir reached the desired temperature, as measured with the external thermocouple.

The figure can be divided into three regions: In the first region, the reservoir thermalizes over a time-scale of approximately 50 min, and the flux stabilized at its equilibrium value, consistent with previous measurements. Nothing unusual occurred during this period. Next, the Rb reservoir is heated to 160 °C, with the shutter still closed. After the Rb reservoir reaches its target temperature, the Li flux gradually decreased, reaching a minimum after around 1 hour. The flux dropped by around 10 %. Following this, the Li flux returned to its equilibrium value over the same time-scale. In the third region, the shutter is opened, allowing the Rb beam to enter the Li reservoir. Despite this, the Li flux does not change.

What is likely happening is that once the Rb reservoir reaches its set temperature, Rb vapor starts to fill the middle section. At the same time, this Rb background is pumped through the Li reservoir into the 6-way cross, as discussed earlier. During this process, Li and Rb atoms appear to collide, reducing the Li flux. After a few hours, the system reaches an equilibrium, with the Li flux returning to its expected equilibrium value. Notably, this behavior was not observed for the Rb beam. Predicting the system's behavior is difficult because both the previous Rb density in the

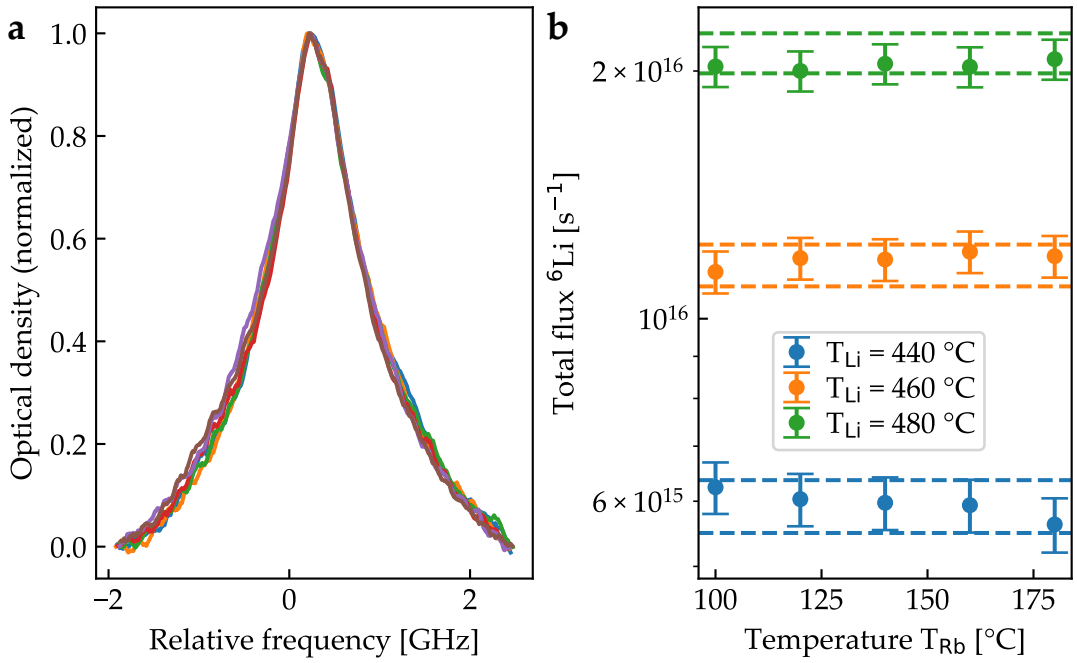

FIGURE 4.12: **a** Normalized optical density spectra for a Li reservoir temperature of 460 ° and different Rb reservoir temperatures. Noise was filtered out using a rolling average for better display. **b** Total flux of Li as a function of the Rb reservoir temperature T_{Rb} for different Li reservoir temperatures T_{Li}. The measurement is performed in a way to minimize the impact of the Rb background, isolating the effect of the collimated Rb beam itself. Details are provided in the text.

middle section and the temperatures of both reservoirs play a role.

It was also observed that the equilibrium was reached faster at higher Li reservoir temperatures. Therefore, the total flux was measured with an open shutter as a function of the Rb reservoir temperature, starting at the highest temperature and waiting for some time before taking measurements. This minimized the impact of the Rb background, isolating the effect of the collimated Rb beam. The results are shown in Fig. 4.12. Fig. 4.12a shows optical density spectra for a Li reservoir temperature of 460 °C and different Rb reservoir spectra, Fig. 4.12b shows the total flux of Li atoms as a function of the Rb reservoir temperature for different Li reservoir temperatures. The beam divergence and the total flux remain unchanged, indicating that the collimated Rb beam does not influence the Li beam, as expected.

Chapter 5

Summary & Outlook

Summary In this theses, a single effusive atomic beam source for the generation of an overlapping beam of lithium and rubidium was presented. The idea behind the source is to implement a series connection of two independent reservoirs for both elements, allowing the source to be operated in either single-species operation or dual-species operation.

First, the experimental setup and its construction were described, with a special focus on the particularities of handling lithium, such as the necessary bakeout of the system due to the storage of lithium chunks in mineral oil, as well as the chemical reactions of lithium with glass.

The main focus of this work was on the characterization of the beam using linear absorption spectroscopy on the D_2 line of both elements, specifically of the two isotopes ^{6}Li and ^{87}Rb, which will be used in the future main experiment. The key quantities determined were the total flux and the beam divergence.

Spectroscopy on lithium showed that the beam performed as predict by theory. A total flux of $1.3 \cdot 10^{16}\,\mathrm{s}^{-1}$ and a $1/e^2$ divergence angle of $2 \cdot 574\,\mathrm{mrad}$ were measured at a reservoir temperature of 450 °C. Considering the geometry of the vacuum system of the main experiment, an estimate of the MOT loading rate was made. At this temperature, this estimate is $1.7 \cdot 10^{10}\,\mathrm{s}^{-1}$. The lifetime of the source was estimated to around 15 000 hours.

Spectroscopy on rubidium showed that there is a flaw in the original design, as the measured flux was two orders of magnitude smaller than expected. The issue was identified in the nozzle design, and the the setup was modified accordingly. The rubidium beam exits the source as a collimated beam with a total flux of $3.3 \cdot 10^{10}\,\mathrm{s}^{-1}$ at 120 °C and a total divergence angle of $2 \cdot 10.3\,\mathrm{mrad}$. The measured flux is a factor of four smaller than the theoretical expectation, and the origin of this discrepancy is not fully understood. The most likely explanation is the formation of background rubidium in the system. The total flux, together with the beam divergence, translates into an estimated MOT loading rate of $9.6 \cdot 10^8\,\mathrm{s}^{-1}$ and a source lifetime of approximately 3900 hours.

In dual-species operation, it was shown that the flux of rubidium drops to half its value at a lithium reservoir temperature of around 400 °C, independent of the rubidium reservoir temperature. An estimated MOT loading rate of at least $4.8 \cdot 10^8\,\mathrm{s}^{-1}$ for ^{87}Rb and at least $2.7 \cdot 10^9\,\mathrm{s}^{-1}$ for ^{6}Li is achievable simultaneously, though an increase in lithium flux must be traded against a decrease in rubidium flux and vice versa. Alternatively, the rubidium reservoir temperature could be increased to boost the rubidium flux while maintaining the lithium flux, but this would drastically reduce the lifetime of the source. For the lithium flux, it was found that the collimated rubidium beam does not affect the total lithium flux, but the rubidium background does. The beam divergence of both beams is not influenced in the dual-species operation.

In conclusion, the lithium beam provides a sufficiently high estimated MOT loading rate for ultra-cold Fermi gas experiments, while the rubidium flux should ideally be higher. In the current rubidium experiment, the MOT loading rate is approximately four times larger than the new source would deliver. A further increase in flux is currently only possible by significantly reducing the lifetime of the source. In dual-species operation, a decent flux of both elements simultaneous was shown to be achievable in this setup.

Outlook A significant issue with this source is the rubidium background in the middle section, which not only affects the pump performance of the ion pump in the long-term, but also affects the operation of the source. It was shown that the background leads to non-trivial, non-equilibrium dynamics in the dual-species operation over a time-scale of hours, making controlled operation of the source challenging. Additionally, it is suspected that this background contributed to the reduced measured rubidium flux. Therefore, a cold nozzle, as already present in the current main experiment, must be implemented in the middle section to reduce the vapor pressure of rubidium.

To further increase the rubidium flux, it is planned to employ transverse cooling in the middle section to reduce the atomic beam divergence, thereby increasing the total flux in the collimated beam after the exit nozzle. Simulations of the achievable increase and the optimal parameters still need to be performed. An additional transversal cooling stage can also be added for lithium to either increase the flux or alternatively extend the lifetime.

It is planned that this upgrades are first tested in a second generation test setup. If successful, the new dual-species source will replace the old one at the main experiment. This replacement can be done without affecting the vacuum in the Zeeman slower and MOT chamber, thanks to a gate valve installed between the source and Zeeman slower and the atomic beam source. Simultaneously, the new laser systems for laser cooling of lithium must be prepared. Once these ugrades are complete, the system will be ready for intriguing experiments.

Appendix A

Angular distribution via effusion from a cylindrical tube

For a cylindrical orifice with non-negligible length, one can distinguish two angular regions of the atomic beam. For $\tan(\theta) < d/L$, there are contributions from both the reservoir and diffusion from the orifice wall. For $\tan(\theta) \geq d/L$, only contributions from the wall are geometrically possible. Consequently, the $\cos(\theta)$ angular distribution of atoms from the thin-walled orifice gets modified by a correction factor $C_0(\theta,\beta)$ where $\beta = d/L$ is the inverse aspect ratio of the tube. For $\tan(\theta) < d/L$, the correction factor is given by

$$C_0(\theta,\beta) = \alpha + \frac{2}{\pi} \cdot \left[(1-\alpha) \left(\arccos(q) - q\sqrt{1-q^2} \right) + \frac{2(1-2\alpha)}{3q} \left(1 - \sqrt{(1-q^2)^3} \right) \right], \tag{A.1}$$

and for $\tan(\theta) \geq d/L$ it is given by

$$C_0(\theta,\beta) = \alpha + \frac{4(1-2\alpha)}{3\pi q}, \tag{A.2}$$

where $q = \tan(\theta)/\beta$ and

$$\alpha = \frac{1}{2} - \frac{1}{3\beta^2} \left[\frac{1 - 2\beta^3 + (2\beta^2 - 1)\sqrt{1+\beta^2}}{\sqrt{1+\beta^2} - \beta^2 \left[\ln(\sqrt{1+\beta^2}+1) - \ln(\beta) \right]} \right]. \tag{A.3}$$

The equations are based on [18]. The angular distribution $C_0(\theta, L/d) \cdot \cos(\theta)$ for different aspect ratios is shown in Fig. 2.2.

Bibliography

1. Giorgini, S., Pitaevskii, L. P. & Stringari, S. Theory of ultracold atomic Fermi gases. *Reviews of Modern Physics* **80,** 1215–1274 (2008).
2. Fröhlich, H. Electrons in lattice fields. *Advances in Physics* **3,** 325–361 (1954).
3. Huang, E. W., Sheppard, R., Moritz, B. & Devereaux, T. P. Strange metallicity in the doped Hubbard model. *Science* **366,** 987–990 (2019).
4. Dutta, O., Gajda, M., Hauke, P., Lewenstein, M., Lühmann, D.-S., Malomed, B. A., Sowiński, T. & Zakrzewski, J. Non-standard Hubbard models in optical lattices: a review. *Reports on Progress in Physics* **78,** 066001 (2015).
5. Feynman, R. P. Simulating physics with computers. *International Journal of Theoretical Physics* **21,** 467–488 (1982).
6. Boll, M., Hilker, T. A., Salomon, G., Omran, A., Nespolo, J., Pollet, L., Bloch, I. & Gross, C. Spin-and density-resolved microscopy of antiferromagnetic correlations in Fermi-Hubbard chains. *Science* **353,** 1257–1260 (2016).
7. Brown, P. T., Mitra, D., Guardado-Sanchez, E., Nourafkan, R., Reymbaut, A., Hébert, C.-D., Bergeron, S., Tremblay, A.-M., Kokalj, J., Huse, D. A., *et al.* Bad metallic transport in a cold atom Fermi-Hubbard system. *Science* **363,** 379–382 (2019).
8. Böttcher, F., Schmidt, J.-N., Hertkorn, J., Ng, K. S., Graham, S. D., Guo, M., Langen, T. & Pfau, T. New states of matter with fine-tuned interactions: quantum droplets and dipolar supersolids. *Reports on Progress in Physics* **84,** 012403 (2020).
9. Veit, C, Zuber, N, Herrera-Sancho, O., Anasuri, V., Schmid, T, Meinert, F, Löw, R & Pfau, T. Pulsed ion microscope to probe quantum gases. *Physical Review X* **11,** 011036 (2021).
10. Zuber, N., Anasuri, V. S., Berngruber, M., Zou, Y.-Q., Meinert, F., Löw, R. & Pfau, T. Observation of a molecular bond between ions and Rydberg atoms. *Nature* **605,** 453–456 (2022).
11. Zou, Y.-Q., Berngruber, M., Anasuri, V. S., Zuber, N., Meinert, F., Löw, R. & Pfau, T. Observation of vibrational dynamics of orientated Rydberg-atom-ion molecules. *Physical Review Letters* **130,** 023002 (2023).
12. Berngruber, M., Bosworth, D. J., Herrera-Sancho, O. A., Anasuri, V. S., Zuber, N., Hummel, F., Krauter, J., Meinert, F., Löw, R., Schmelcher, P., *et al.* In Situ Observation of Nonpolar to Strongly Polar Atom-Ion Collision Dynamics. *Physical Review Letters* **133,** 083001 (2024).
13. Tomza, M., Feldker, T., Furst, H., Hirzler, H., Ewald, N., Mazzanti, M., Wiater, D. & Gerritsma, R. *Buffer gas cooling of a trapped ion to the quantum regime* in *APS Division of Atomic, Molecular and Optical Physics Meeting Abstracts* **2020** (2020), T03–001.

14. Schmid, T, Veit, C, Zuber, N, Löw, R, Pfau, T, Tarana, M & Tomza, M. Rydberg molecules for ion-atom scattering in the ultracold regime. *Physical review letters* **120,** 153401 (2018).
15. Marti, G. E., Olf, R., Vogt, E., Öttl, A. & Stamper-Kurn, D. M. Two-element Zeeman slower for rubidium and lithium. *Physical Review A—Atomic, Molecular, and Optical Physics* **81,** 043424 (2010).
16. Bowden, W., Gunton, W., Semczuk, M., Dare, K. & Madison, K. W. An adaptable dual species effusive source and Zeeman slower design demonstrated with Rb and Li. *Review of Scientific Instruments* **87** (2016).
17. Schmid, T. *Rydberg Molecules for Ultracold Ion-Atom Scattering* PhD thesis (University of Stuttgart, 2019).
18. Halwidl, D. *Development of an effusive molecular beam apparatus* (Springer, 2016).
19. Ramsey, N. *Molecular beams* (Oxford University Press, 1956).
20. Massey, H. & Mohr, C. Free paths and transport phenomena in gases and the quantum theory of collisions. II.—The determination of the laws of force between atoms and molecules. *Proceedings of the Royal Society of London. Series A, Containing Papers of a Mathematical and Physical Character* **144,** 188–205 (1934).
21. Kennard, E. H. *et al. Kinetic theory of gases* (McGraw-hill New York, 1938).
22. Howard, W. M. Density field for rarefied flow through an orifice. *The Physics of Fluids* **4,** 521–524 (1961).
23. Herman, M. A. & Sitter, H. *Molecular beam epitaxy: fundamentals and current status* (Springer Science & Business Media, 2012).
24. Foot, C. J. *Atomic physics* (Oxford university press, 2005).
25. Steck, D. A. Rubidium 85 D Line Data (2008).
26. Gehm, M. E. Properties of 6 Li.
27. Steck, D. A. Rubidium 87 D Line Data (2001).
28. Alcock, C. B., Itkin, V. & Horrigan, M. Vapour pressure equations for the metallic elements: 298–2500K. *Canadian Metallurgical Quarterly* **23,** 309–313 (1984).
29. Derevianko, A., Porsev, S. G. & Babb, J. F. Electric dipole polarizabilities at imaginary frequencies for hydrogen, the alkali–metal, alkaline–earth, and noble gas atoms. *Atomic Data and Nuclear Data Tables* **96,** 323–331 (2010).
30. Stan, C. A. & Ketterle, W. Multiple species atom source for laser-cooling experiments. *Review of scientific instruments* **76** (2005).
31. Conrad, R. *Design and setup of a Rb-Li dual-species vapor source for an ultracold atoms experiment* MA thesis (University of Hamburg, 2023).
32. Jenninger, B. & Chiggiato, P. CAS tutorial on RGA Interpretation of RGA spectra. *CERN Accelerator School: Vacuum for Particle Accelerators, Glumslov, Sweden* **6** (2017).
33. Fang, Z., Cai, H., Chen, G. & Qu, R. *Single frequency semiconductor lasers* (Springer, 2017).
34. Demtröder, W. *Laserspektroskopie: Grundlagen und Techniken* (Springer-Verlag, 2007).
35. Wodey, E, Rengelink, R., Meiners, C, Rasel, E. & Schlippert, D. A robust, high-flux source of laser-cooled ytterbium atoms. *Journal of Physics B: Atomic, Molecular and Optical Physics* **54,** 035301 (2021).

36. Rothe, E. W. & Bernstein, R. B. Total collision cross sections for the interaction of atomic beams of alkali metals with gases. *The Journal of Chemical Physics* **31,** 1619–1627 (1959).